

2019-03

Internal lee waves and baroclinic bores over a tropical seamount shark 'hot-spot'

Hosegood, Philip

<http://hdl.handle.net/10026.1/13205>

10.1016/j.pocean.2019.01.010

Progress in Oceanography

Elsevier

All content in PEARL is protected by copyright law. Author manuscripts are made available in accordance with publisher policies. Please cite only the published version using the details provided on the item record or document. In the absence of an open licence (e.g. Creative Commons), permissions for further reuse of content should be sought from the publisher or author.

1 Internal lee waves and baroclinic bores over a
2 tropical seamount shark 'hot-spot'

3
4
5 **P.J. Hosegood^{1*}**

6 W. A. M. Nimmo-Smith¹

7 R. Proud²

8 K. Adams³

9 A. S. Brierley²

10
11 ¹Marine Institute and School of Biological and Marine Science,
12 University of Plymouth,
13 Drake Circus,
14 Plymouth
15 Devon, PL4 8AA

16
17 ²Pelagic Ecology Research Group,
18 Scottish Oceans Institute,
19 Gatty Marine Laboratory,
20 University of St Andrews,
21 Fife KY16 8LB

22
23 ³Scripps Institution of Oceanography,
24 University of California,
25 San Diego,
26 La Jolla,
27 California, USA8

28
29 *Corresponding author: Phil Hosegood, phil.hosegood@plymouth.ac.uk

30
31 Declarations of interest: None

Abstract

Oceanographic observations were made with a subsurface oceanographic mooring over the summit and flanks of two neighbouring seamounts in the tropical Indian Ocean to identify processes that may be responsible for the aggregation of silvertip sharks (*Carcharhinus albimarginatus*) in the deep water drop-off surrounding the summits. The seamounts, which are in the Chagos Archipelago in the British Indian Ocean Territories, are narrow in horizontal extent (<10 km), have steeply sloping (>15°) sides that rise from depths of >600 m, and flat summits at a depth of 70 m. They are subjected to forcing at subinertial, basin-scales and local scales that include a mixed tidal regime and storm-generated near inertial waves. At the drop-off, at a depth of between 70 – 100 m, isotherms oscillate at both diurnal and semidiurnal frequencies with amplitudes of ~20-30 m. The waves of tidal origin are accompanied by short period (~5 minutes) internal waves with amplitudes $O(10\text{ m})$ and frequencies close to the local buoyancy frequency, N , within the thermocline which is the maximum frequency possible for freely propagating internal waves. The tidal oscillations result from internal lee waves with 30 m vertical wavelength generated by the prevailing currents over the supercritical seamount flanks, whereby the bottom slope is greater than the internal tide wave slope. The 'near- N ' waves are due to enhanced shear associated with the hydraulic jumps that form from the lee waves due to the abrupt transition from steeply sloping sides to a relatively flat summit. The jumps manifest themselves as bottom-trapped bores that propagate up the slope towards the summit. Further observations over the summit reveal that the bores subsequently flush the summits with cold water with tidal periodicity. The bores, which have long wave phase speeds more than double that of the bore particle velocities, are characterised by intense vertical velocities ($>0.1\text{ m s}^{-1}$) and inferred local resuspension but relatively little turbulence based on temperature overturns. Our results strongly implicate lee waves as the dynamic mechanism of leading order importance to the previously observed accumulation of biomass adjacent to the supercritical slopes that are commonplace throughout the archipelago. We propose that further investigation should identify the spatiotemporal correlation between internal wave activity and fish schooling around the summit, and whether such schooling attracts predators.

Keywords: Chagos Archipelago; Indian Ocean; lee waves; seamount; apex predators; internal waves

66 **1. INTRODUCTION**

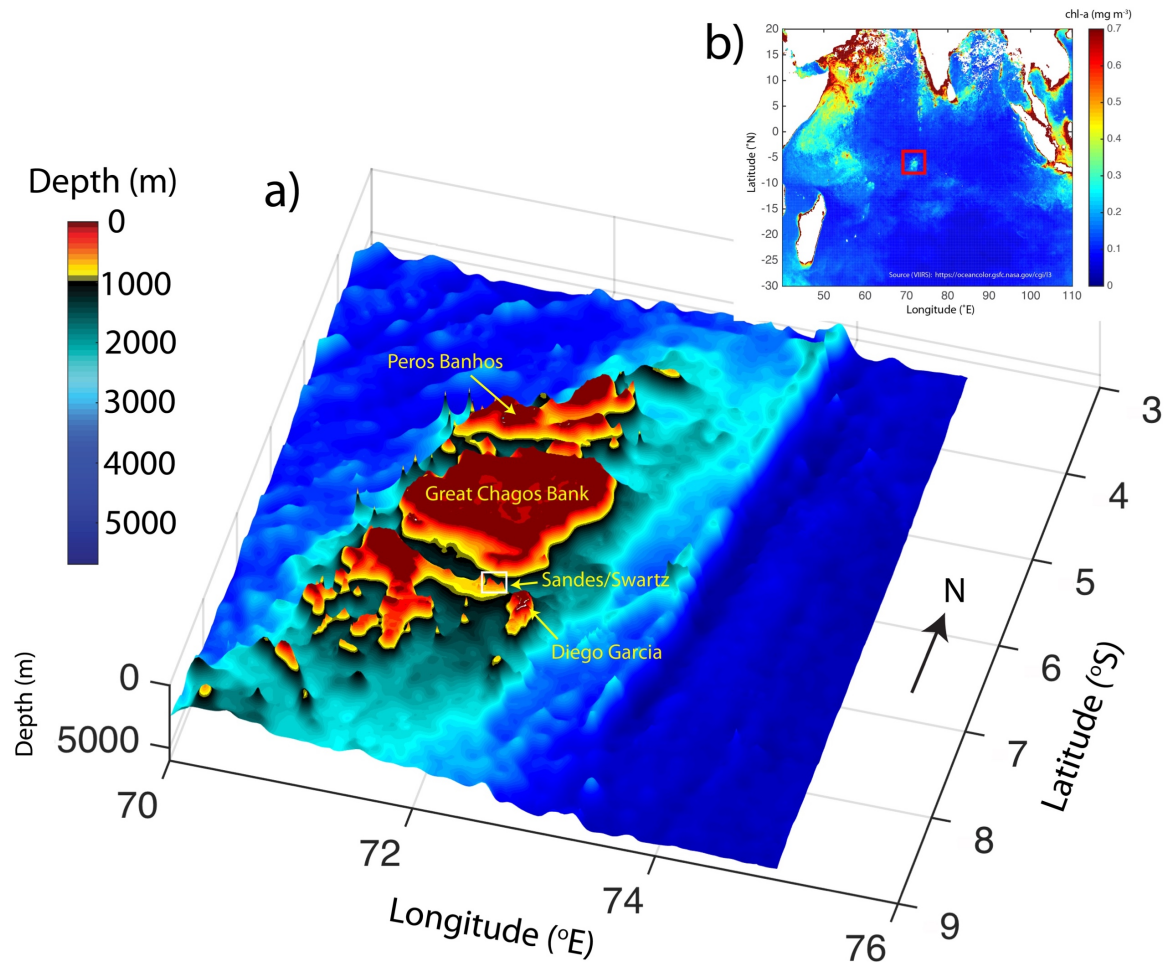
67

68 The Chagos Archipelago (Figure 1) is located within the central Indian Ocean and
69 hosts the world's second largest no-take Marine Protected Area (MPA). It is
70 considered a 'hotspot' of marine biodiversity and abundance, with coral reef fish
71 abundance an order of magnitude higher than other areas of the Indian Ocean
72 (Sheppard et al. 2012). Within a largely oligotrophic ocean (Morel et al. 2010), the
73 archipelago is readily visible in remotely sensed images of chlorophyll-a (Figure 1b),
74 suggestive of local processes sustaining higher levels of primary production than
75 those observed in the surrounding ocean. Recent surveys also demonstrate that
76 higher trophic levels, in particular shark species including silvertips, grey reef and
77 scalloped hammerhead, that are not directly dependent on primary production, are
78 also especially abundant throughout the region, particularly over shallow topography
79 (Letessier et al. 2016; Tickler et al. 2017).

80

81 Whilst the archipelago is subject in a regional sense to the influence of a range of
82 basin-scale oceanographic processes, including the Indian Ocean Dipole (IOD)
83 (Praveen Kumar et al. 2014), the Madden Julian Oscillation (MJO)(Vialard et al.
84 2008), equatorial Rossby waves (Webber et al. 2014) and the monsoon (Hermes
85 and Reason 2008), at a more local scale the role of flow-topography interaction
86 becomes important due to the steeply sloping topography. Given the remote location
87 of the archipelago, there have been no detailed physical oceanographic
88 measurements made to date that enable an identification of the dominant dynamics
89 and how they impact on the marine ecosystem, particularly the concentration of
90 biomass at topographic features as observed by Letessier et al. (2016). Due to the
91 archipelago's volcanic origins, the seafloor topography throughout the British Indian
92 Ocean Territories (BIOT) is characterised by numerous seamounts and banks
93 flanked by steeply sloping sides. To assess the efficacy of the MPA in sustaining
94 ocean life, there is a need to understand the processes, both regional and local
95 scale, that may promote production and biodiversity throughout the region and how
96 such mechanisms might sustain the observed high abundance of species that reside
97 there.

98



99

100 *Figure 1. a) Depth chart of the Chagos Archipelago in the British Indian Ocean Territory, indicating the position of the*
 101 *seamounts considered in this paper, Sandes and Swartz, located approximately 10 nautical miles north west of Diego*
 102 *Garcia, and b) the January–mean chlorophyll-a over a 20 year period throughout the Indian Ocean with the location of the*
 103 *Chagos Archipelago indicated by the red box.*

104 Due to the protected status of BIOT, it is of particular interest whether discrete
 105 features within the archipelago such as seamounts and isolated submarine banks
 106 play a disproportionate role in, firstly, potentially promoting primary production
 107 through the injection of nutrients to the euphotic zone and, secondly, acting as a
 108 refuge for apex predators due to as yet unidentified processes. Recent shark
 109 surveys at shallow (<100 m) sites throughout BIOT reveal that shark abundance
 110 increases markedly near such features (Tickler et al. 2017), especially over an
 111 isolated seamount called Sandes where many tens of sharks have been observed to
 112 aggregate around the flanks of the seamount summit but not over the centre (Figure
 113 2). Similarly, acoustic surveys throughout the region showed acoustic backscatter at
 114 38 and 120 kHz, which are rough proxies for fish and zooplankton biomass, within

115 the upper 180 m to be increased by a factor of 100 within 1.6 km of steeply sloping
116 topography relative to the pelagic environment (Letessier et al. 2016). Similar results
117 were found for seamounts throughout the open ocean and suggest higher species
118 diversity to extend 30-40 km from the seamounts (Morato et al. 2010). There is
119 presently little direct observational evidence of the processes responsible for, or
120 contributing to, the aggregation of biomass at steeply sloping topography, particularly
121 at higher trophic levels. The importance of seamounts to apex predators in a
122 conservation context has been recognised in the Coral Sea area of Australia where
123 its seamounts are viewed as an integral component of conservations plans (Barnett
124 et al. 2012). Efforts to design an effective management and conservation plan which
125 may ultimately lead to the creation of an MPA in the Coral Sea have thus been
126 deemed to require an understanding of the spatial ecology of sharks over and
127 around the seamounts. Our goal here, therefore, is to develop our understanding of
128 what physical mechanisms occurring over seamounts may be responsible for the
129 spatial ecology of sharks over Sandes and throughout BIOT more generally, thereby
130 improving our understanding of the sensitivity of such ecosystems to environmental
131 change and anthropogenic pressure in a large MPA.

132
133 The physical mechanisms typically invoked within a conservation context as
134 explaining higher productivity, species diversity and abundance over and around
135 seamounts include, Taylor columns (Genin and Boehlert 1985; Genin 2004; Boehlert
136 1988) internal waves dynamics (Stevens et al. 2014; Van Haren et al. 2017) and
137 upwelling (White and Mohn 2004); biophysical mechanisms further include trophic
138 focussing whereby zooplankton are trapped over shallow topography during daytime
139 when attempting to vertically migrate at dawn (Haury et al. 2000; Stevens et al.
140 2014). Much of the previous observational evidence for such processes has been
141 obtained from large, deep seamounts in relatively weak flow fields where Taylor
142 columns are more likely to occur than over the smaller scale, narrow seamounts
143 found throughout BIOT.

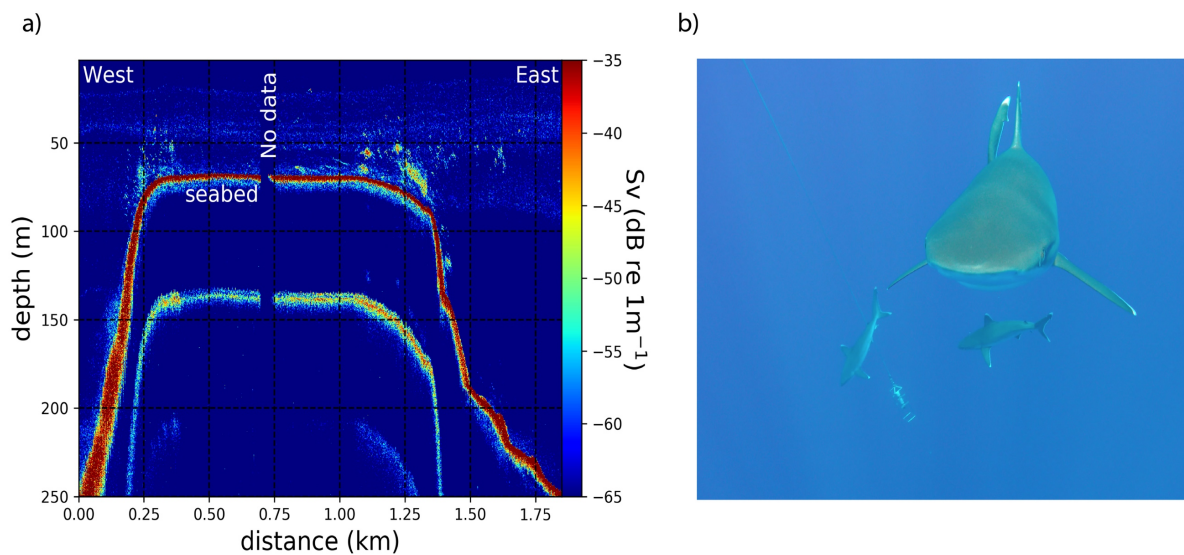
144
145 In most cases, however, direct evidence of the role played by dynamic processes in
146 promoting productivity or interactions between higher trophic levels is lacking.
147 Internal tides have been extensively studied, predominantly over continental slopes
148 where their generation and reflection promotes enhanced turbulent mixing of

149 importance to the global circulation (e.g. Wunsch and Ferrari 2004). In the vicinity of
150 seamounts and submarine banks, internal tides may elevate production by
151 increasing turbulent diffusion of nutrients from the deep ocean into the euphotic zone
152 (e.g. Palmer et al. 2013; Sharples et al. 2013). Similarly, over a seamount in the Mid-
153 Atlantic Ridge, internal wave driven mixing may be responsible for the vertical mixing
154 of oxygen to depths where a sponge belt thrived due to enhanced resuspension of
155 particulate matter on which the sponges depend by internal waves (Van Haren et al.
156 2017). The vertical displacement of isotherms due to internal tides may also impact
157 on vertical distributions of chlorophyll rather than production per se; over Melville
158 Bank in the southern Indian Ocean, the internal tide advects layers of high
159 chlorophyll vertically by 200 m rather than increasing production by supplying
160 nutrients (Pollard and Read 2017). It was speculated, however, that the internal
161 tides, which generate oscillations in temperature over tidal periods of more than 3°C,
162 may also drive the periodic injection of nutrients to the euphotic zone over the
163 summit at seamounts that reach close enough to the surface. Direct nutrient injection
164 through advection may occur more readily in shallower reef environments; the tidally-
165 induced upwelling of nutrient rich water from depth was identified as a potential
166 mechanism for promoting reef growth at Cook's Passage in the Great Barrier Reef
167 (Thompson and Golding 1981) but the observations were unable to resolve the
168 forcing mechanism as internal tides.

169

170 In this paper, we consider the dynamics occurring within BIOT over a pair of recently
171 discovered seamounts, Sandes seamount and a close neighbour, Swart, of almost
172 identical scale and height. We demonstrate that both are effective generators of
173 internal lee waves at tidal frequencies in the precise location where resident silvertip
174 sharks have been observed. We show that the seamount summits, which each reach
175 a depth of 70 m and rise from depths of more than 600 m, are subjected to flushing
176 by internal bores that are generated by the release of internal lee waves over the
177 flanks of the seamounts. Lee waves are formed over especially steep topography,
178 defined as slopes steeper than the characteristic of an internal wave of a given
179 frequency, and manifest themselves as depressed isopycnals on the lee side of a
180 ridge or summit. As the flow forcing the depression of isopycnals weakens or
181 releases, the wave propagates upslope, potentially in the form of a bottom-trapped

182 internal bore (Legg and Klymak 2008). Whilst recent work on lee waves have
 183 focussed on their generation at ridges (Legg and Klymak 2008; Pinkel et al. 2012;
 184 Alford et al. 2014; Buijsman et al. 2014; da Silva et al. 2015), earlier work identified
 185 tall isolated seamounts as effective generators of lee waves that destroy Taylor caps
 186 (Chapman and Haidvogel 1992). Such a mechanism promotes turbulence,
 187 resuspension of material deposited over the seabed and is confined to the top of the
 188 slope; it is demonstrated in this paper that such a mechanism is consistent with the
 189 topography, the forcing, resulting dynamic response, and furthermore occurs in the
 190 same location as where apex predators are concentrated around the summits of the
 191 seamounts.



192
 193 *Figure 2. a) Acoustic backscatter, Sv, from a night-time EK60 (38kHz) transect over the summit of Sandes indicating the*
 194 *aggregation of biomass over the flanks and b) a single frame from visual observations of the silvertip community over the*
 195 *flanks of Sandes seamount during the CTD survey. During multiple excursions into the water, the sharks were only present*
 196 *when the boat was positioned over the steeply sloping sides surrounding the summit where the increased biomass was*
 197 *observed in a). We estimated that, over the flanks of Sandes, there were in excess of 50 sharks typically within view at a*
 198 *given moment.*

199 2. MATERIALS AND METHODS

200
 201 Observations are presented from two multidisciplinary cruises to BIOT aboard the
 202 Fisheries Patrol vessel, the M/V *Pacific Marlin*. The first took place between 10th -
 203 25th January 2015 and the second during the following year between 5th - 24th
 204 February 2016. As such, both cruises took place between the northeast and
 205 southwest monsoons when atmospheric conditions are typically relatively settled.
 206 Whilst this was the case during 2015, the 2016 cruise was subjected to more

207 unsettled conditions although the monthly mean wind speed estimated from the
208 Cross-calibrated Multi-Platform (www.remss.com) remained $<3 \text{ m s}^{-1}$. During both
209 cruises, a storm passed near the site of the mooring at Sandes and Swart, located
210 approximately 30 miles from Diego Garcia (Figure 1a) from which the majority of
211 results are taken in the present paper.

212

213 **2.1 Geophysical context: seamount location and dimensions**

214 Both Sandes and Swart seamounts have almost identical dimensions, rising from
215 depths of $>2000\text{m}$ on their northern flank to 70 m (Figure 3). The pair of neighbouring
216 seamounts lie at the eastern end of a bank of depth $\sim 1000 \text{ m}$; the bank is bordered
217 to the north by a deep channel, one of the numerous deep passages within BIOT
218 whose depths exceed 2000 m and that intersect the various atolls.

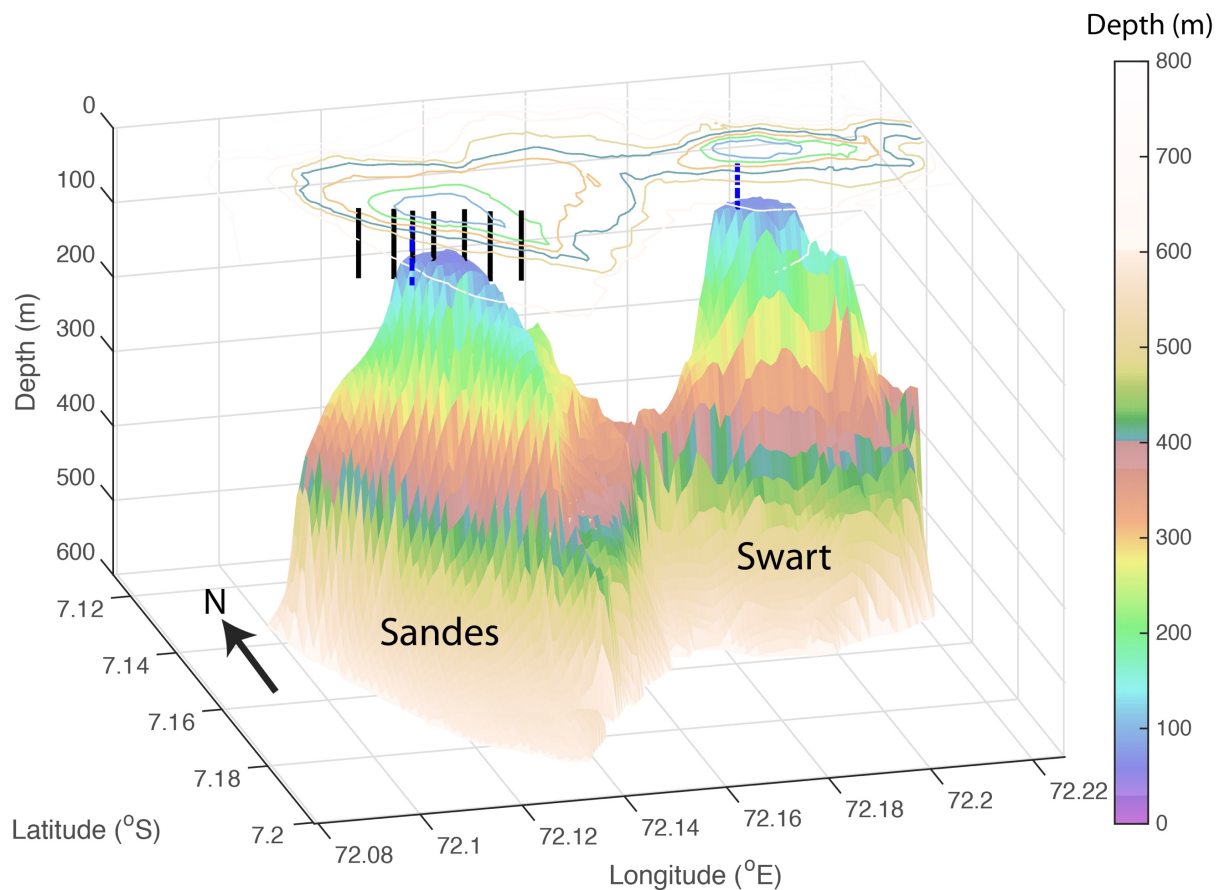
219

220 Each seamount has a short horizontal scale compared to the more heavily studied
221 examples in the literature such as Great Meteor (60 km), Fieberling Guyot (50 km),
222 Cobb (25 km) and Condor Seamounts (40 km). The distance across the seamount at
223 a depth of 600 m, which corresponds to the depth at which the very steeply sloping
224 sides (up to 20°) start to reduce in gradient, is $<10 \text{ km}$. Thus, Sandes and Swart fall
225 into the category of narrow, steep seamounts whose heights are at the lower end of
226 the criteria for defining isolated topographic features as seamounts (nominally
227 defined as features rising more than 1000 m). As both seamounts have almost
228 identical dimensions and bottom slopes, we consider the dynamics (e.g. prevailing
229 tidal regime) occurring at one to be also occurring at the other.

230

231 **2.2 Oceanographic mooring and vessel-based measurements**

232 A mooring was deployed over the flanks of Sandes during the 2015 cruise and over
233 the summit of Swart during 2016. The 2015 mooring was deployed on the western
234 flank of Sandes summit at $7^\circ 9.006'S$, $72^\circ 7.256'E$ in a water depth of 96 m. The
235 2016 mooring was deployed over the centre of the summit of Swart at $7^\circ 8.373'S$,
236 $72^\circ 11.362'E$ in a water depth of 70 m (Figure 3). Both moorings were deployed for
237 14.5 days.



238

239

Figure 3. Bathymetry measured with the EK60 over Sandes (left) and Swart (right) indicating the location of the CTD profiles conducted during 2016 over Sandes (Black lines). The locations and vertical extent of the moorings over both seamounts are indicated by the dashed blue lines. Depth contours are overlain at the surface in 100 m increments.

241

242

The specific mooring configuration for each deployment differed slightly between 2015 and 2016 but in both cases comprised a pair of RDI 600 kHz acoustic Doppler current profilers mounted at mid-depth with one looking upward and the other downward. The ADCPs provided near full water-column coverage when sampling in 1 m vertical bin sizes and in 3 second ensembles. In the analysis that follows we consider the barotropic currents defined as the depth mean currents and the baroclinic components as the observed currents minus the barotropic component.

249

250

Seabird SBE56 temperature sensors were mounted on the mooring line with a vertical spacing of either 2 or 4 m during 2015 and 2 m during 2016. Sensors sampled at 1 Hz with an accuracy of 0.002°C. Temperature measurements were complemented by RBR conductivity-temperature-depth (CTD) sensors, also sampling at 1 Hz, mounted at the bottom, mid-depth and towards the surface (20 m depth in 2015, 10 m depth in 2016). The upper CTD in each case enabled an

255

256 assessment of the vertical displacement arising from mooring knockdown due to
257 drag of the mooring elements in the currents (which were $<0.4 \text{ m s}^{-1}$), particularly the
258 uppermost buoyancy which comprised in 2015 of a single subsurface buoy with 50
259 kg buoyancy and two of the same buoys in 2016. Data have been interpolated to
260 regularly spaced heights above the seabed expressed in metres above bottom
261 (mab).

262
263 Vertical profiles were acquired at regular intervals throughout both cruises with a RBR
264 Concerto (2015) or Maestro (2016) CTD sensor sampling at 6 Hz (2015) and 12 Hz
265 (2016). The Maestro was further integrated with a Rinko dissolved oxygen sensor and
266 Seapoint chlorophyll-a fluorometer.

267
268 A brief CTD survey using a RBR Concerto sampling at 1 Hz was undertaken over the
269 summit of Sandes during 2016 (indicated by the black solid lines in Figure 3). The
270 survey comprised two transects over the summit during each of which 7 profiles were
271 acquired to a depth of almost 100 m. As the two transects were separated by half of a
272 semidiurnal tidal cycle, the difference between the two transects demonstrates the
273 tidal influence on water properties over the seamount summit and flanks.

274
275 Bathymetry data were obtained from repeated transects with the Simrad EK60
276 echosounder operating at 38 and 120 kHz that were conducted to map the spatial and
277 temporal distribution of biomass around the seamounts. Point measurements of depth
278 were gridded to a regular grid with 100 m horizontal resolution.

279 280 **2.3 Remote sensing and regional climate indices**

281 Sea surface height and derived products including surface geostrophic velocities and
282 their anomalies computed from a 20-year mean were obtained at 0.25° resolution
283 from www.marine.copernicus.eu. Sea surface temperature was measured by the
284 MODIS sensor and obtained from the Jet Propulsion Laboratory website
285 (<https://podaac.jpl.nasa.gov/>). The data are used to demonstrate the difference in
286 regional conditions between the two mooring deployments in 2015 and 2016.

287 288 **2.4 Data Handling**

289 **2.4.1 Tidal Analysis**

290 To isolate the tidal contribution to the observed currents, harmonic analysis
291 (Pawlowicz et al. 2002) was used to identify the deterministic barotropic or phase-
292 locked baroclinic currents in the ADCP data. Incoherent (baroclinic) internal waves
293 that are not phase-locked lead to a smearing of energy around the primary tidal
294 frequency (Hosegood and van Haren 2006). Predicted tidal velocities are estimated
295 using those tidal constituents with a signal-to-noise ratio >2 and at depths for which
296 the predicted ellipse properties exceed the predicted 95% confidence interval. A lack
297 of daytime scatterers in the lower 30 m at Sandes resulted in intermittent missing
298 data during times of sunlight, precluding the determination of the periodic tidal
299 contribution by harmonic analysis. As a result, there are no reliable tidal velocity
300 predictions at Sandes below depths of ~ 60 m.

301

302 **2.4.2 Shear instability estimates**

303 The internal wave processes studied in this paper lend themselves to the promotion
304 of turbulent mixing by shear instability. To assess the likelihood of shear instability,
305 the Richardson number, $Ri = N^2/S^2$ where $N^2 = (-g/\rho_0)/(\partial\rho/\partial z)$ is the buoyancy
306 frequency squared, g is the gravitational acceleration and ρ_0 is a reference density,
307 and $S^2 = ((\partial u/\partial z)^2 + (\partial v/\partial z)^2)$, where u and v are the eastward and northward
308 velocities, respectively was estimated and for which instability is expected when $Ri <$
309 0.25 (Turner, 1973). Shear was computed over the 1 m vertical intervals
310 corresponding to the ADCP bin sizes following smoothing with a 3 point running
311 average filter.

312

313 In the absence of vertical profiles of density, density was estimated from the
314 temperature profile after applying the T-S relationship derived from the CTD profile
315 acquired adjacent to Sandes during 2016 at the time of the mooring deployment. The
316 T-S relationship was observed to be very stable throughout the archipelago during
317 both 2015 and 2016. Stratification was estimated from temperature measured by the
318 sensors spaced between 2-5 m apart and subsequently interpolated to 1 m intervals
319 to match the velocity data. Both shear and stratification were interpolated to the
320 same times with 10 second resolution between estimates.

321

3. INTERNAL TIDES AND LEE WAVES OVER SEAMOUNTS

The narrow and steep seamounts studied here are less susceptible to slow and steady perturbations to the mean flow and more likely to be influenced by internal wave-related processes. Stratification supports the propagation of internal waves between frequencies $f < \sigma < N$, where $f = 2\Omega \sin \phi$ is the local Coriolis frequency, which is twice the local vertical component of the Earth's rotation vector, Ω , at latitude ϕ ($1.77 \times 10^{-5} \text{ s}^{-2}$ at 7°S). Previous observations have demonstrated predator foraging over submerged banks to be closely related to the timing of internal lee wave formation and their release following the reversal of the forcing tidal currents (Jones et al. 2014). In this section we demonstrate the favourable geometry and oceanographic conditions for the generation of similar features to provide the context for interpreting the results in following sections.

The sloping flanks of seamounts and neighbouring banks promote the generation of linear, feely propagating internal tides by interaction between the barotropic tide and stratification. Internal tides are generated most efficiently at the location where the bottom slope, γ , matches the angle with respect to the horizontal of the slope, s ,

$$s = \sqrt{\frac{\sigma^2 - f^2}{N^2 - f^2}}$$

of an internal wave with frequency σ (LeBlond and Mysak 1978). In a continuously stratified fluid, beams of internal tidal energy are predicted to radiate away from the source region where elevated near-bed shear and dissipation is expected.

For supercritical topography, whereby the bottom slope exceeds s , lee waves may form on the downstream side of isolated topography and propagate back upstream as the flow weakens and, potentially reverses. Lee waves are formed at the top of the slope when the lee wave frequency $\sigma_{lee} = N\beta > 2\sigma_o$, where $\beta = h_o/W$ is the aspect ratio of the topography, h_o is the seamount height and W its width, is greater than the forcing frequency, σ_o , which here is assumed to be the tide (Legg and Klymak 2008).

353 In our observations, $\sigma_{lee} \sim 0.002 \text{ s}^{-1}$, which is more than an order of magnitude larger
354 than that of the M_2 tide, $\sigma_0 = 1.4 \times 10^{-4} \text{ s}^{-1}$.

355

356 Additional nondimensional parameters quantifying the susceptibility to lee wave
357 generation include the topographic steepness, defined here as $\alpha = \gamma/s$. For $h_0 = 600 \text{ m}$
358 and $W = 3000 \text{ m}$ and N taken from the CTD profile acquired adjacent to Sandes, 10
359 $< \alpha < 61$ with a mean value of 25, significantly higher than the critical value of unity
360 (which essentially determines the transition to supercritical slopes). The value of the
361 parameter $h_0/W = 0.2$ estimated here is exactly the same as that used by Legg and
362 Klymak (2008) in their ‘steep’ simulations. Sandes and Swart seamounts are thus
363 expected to block the incident flow and generate lee waves on the downstream
364 flanks. The steepness of the sloping flanks compared to the wave slope
365 concentrates the elevated dissipation associated with the lee wave at the top of the
366 slope rather than over a wider area of seabed extending downslope (Klymak et al.
367 2010b).

368

369 The lee wave formation is associated with the depression of isotherms on the
370 downstream side of the obstacle; as the flow slackens and even reverses as would
371 be the case for an oscillatory tide, the isotherms rebound and generate a wave that
372 propagates upwards. When both the flanks are supercritical and the top of the slope
373 is critical, i.e. $\lambda = s$, is satisfied, nonlinear internal bores develop that propagate along
374 the bed over the top of the slope (Legg and Huijts 2006). The degree of nonlinearity
375 in the lee waves formed is predicted by the topographic Froude number,

376

377

$$Fr = \frac{U_0}{Nh_0}$$

378

379 for which the incident flow is blocked by the topographic obstacle and nonlinear lee
380 waves and internal hydraulic jumps are predicted when $Fr < 1$ (Mayer and Fringer
381 2017). Here, $Fr = 0.017$ for $U_0 = 0.2 \text{ m s}^{-1}$, $N = 4 \times 10^{-2} \text{ s}^{-1}$, which are typical values for
382 the current case based on the observed CTD profiles and velocity time series. For
383 other realistic parameter values, Fr is generally always < 0.1 . For such small Fr , the
384 vertical scale of the lee wave scales as $\lambda_z/2 \approx \pi U_0/N$ (Klymak et al. 2010a). The

385 waves are 'high mode' and therefore of small vertical scale, dissipate energy locally
386 and have the further consequence that any tidal beam escaping the seamount is
387 more diffuse than would otherwise be the case in the absence of local dissipation of
388 high modes.

389

390 Hydraulic jumps form where the flow transitions from supercritical, whereby the
391 internal wave phases speed c ,

392

393
$$c = \left[\frac{g' H_1 H_2}{(H_1 + H_2)} \right]^{1/2}$$

394

395 where $g' = g(\rho_2 - \rho_1)/\rho_2$, with ρ_i the density for the respective layer, $i = 1, 2$ (Henyey and
396 Hoering 1997), is less than the current velocity, i.e. $U/c > 1$, to subcritical as it flows
397 downslope. The implication is that the depth change during the tidal period is large,
398 expressed as;

399

400
$$\frac{N}{\sigma_{M2}} \frac{dh}{dx} > 1$$

401

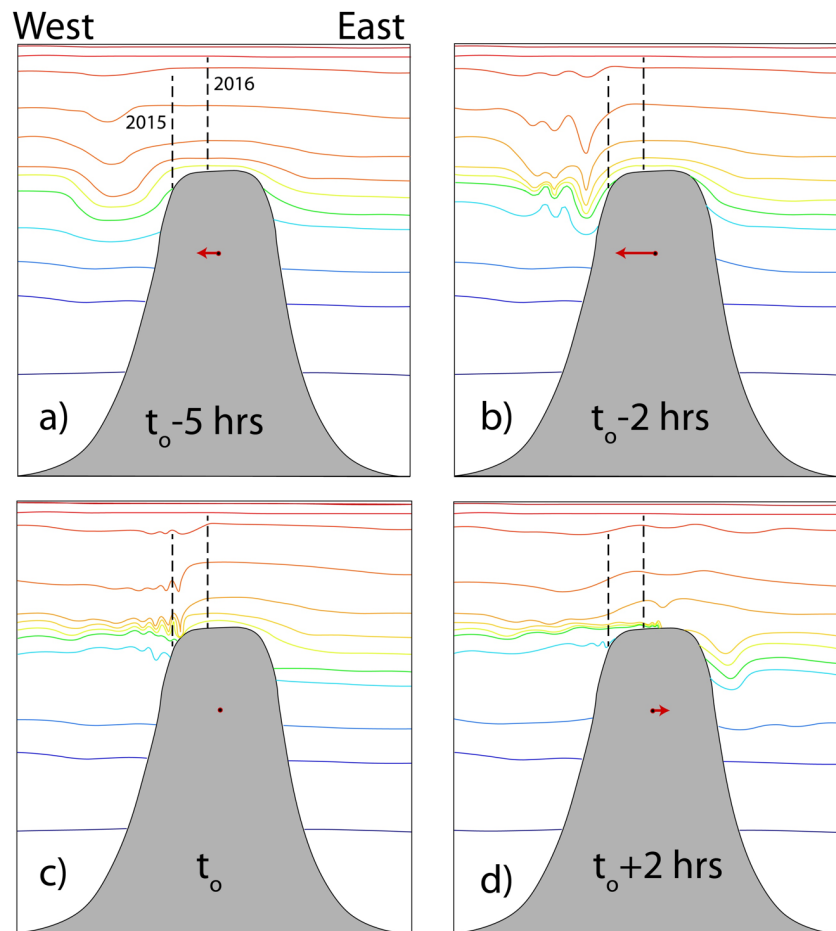
402 For $N = 4 \times 10^{-2} \text{ s}^{-1}$ and $dh/dx = 0.25$ over the steeply sloping sides of Sandes and
403 Swart, we obtain values of 71, indicating that the depth change is easily capable of
404 supporting the development of a hydraulic jump during the downslope flow.

405

406 Theory thus indicates that the flanks of Sandes and Swart are steep compared to the
407 slope of internal tidal waves, rendering them conducive to the generation of internal
408 lee waves on their downstream sides and the generation of internal bores as the tide
409 weakens and reverses.

410 Figure 4 illustrates the evolution of the density field over the summit of Sandes and
411 Swart throughout the tidal cycle. Note that the lee wave formation mechanism is
412 more complicated when a persistent, unidirectional background current is present
413 with an amplitude equal to or exceeding the tidal forcing; under such circumstances,

414 the current depressing isotherms on the downstream may not reverse with the tide
 415 such that the rebounding of isotherms onto the summit may not occur (
 416 Figure 4c,d)



417
 418 Figure 4. Cartoon demonstrating in two dimensions the lee wave generation during (a-b)
 419 westward flow and its evolution into an internal bore that propagates onto the seamount
 420 summits as (c-d) the flow weakens and reverses. Typical timescales are indicated at the
 421 bottom of each panel. The red arrow superimposed on the seamount indicates the direction
 422 of flow, here assumed to be purely east-west. The vertical black dashed lines illustrate the
 423 relative position of the moorings presented in this paper; the 2015 mooring was deployed
 424 on the flank of Sandes and the 2016 mooring on the summit of Sandes.

426 **4. RESULTS**

428 **4.1 Oceanographic context**

430 **4.1.1 Regional conditions: Geostrophic currents and Sea Surface**

431 **Temperature**

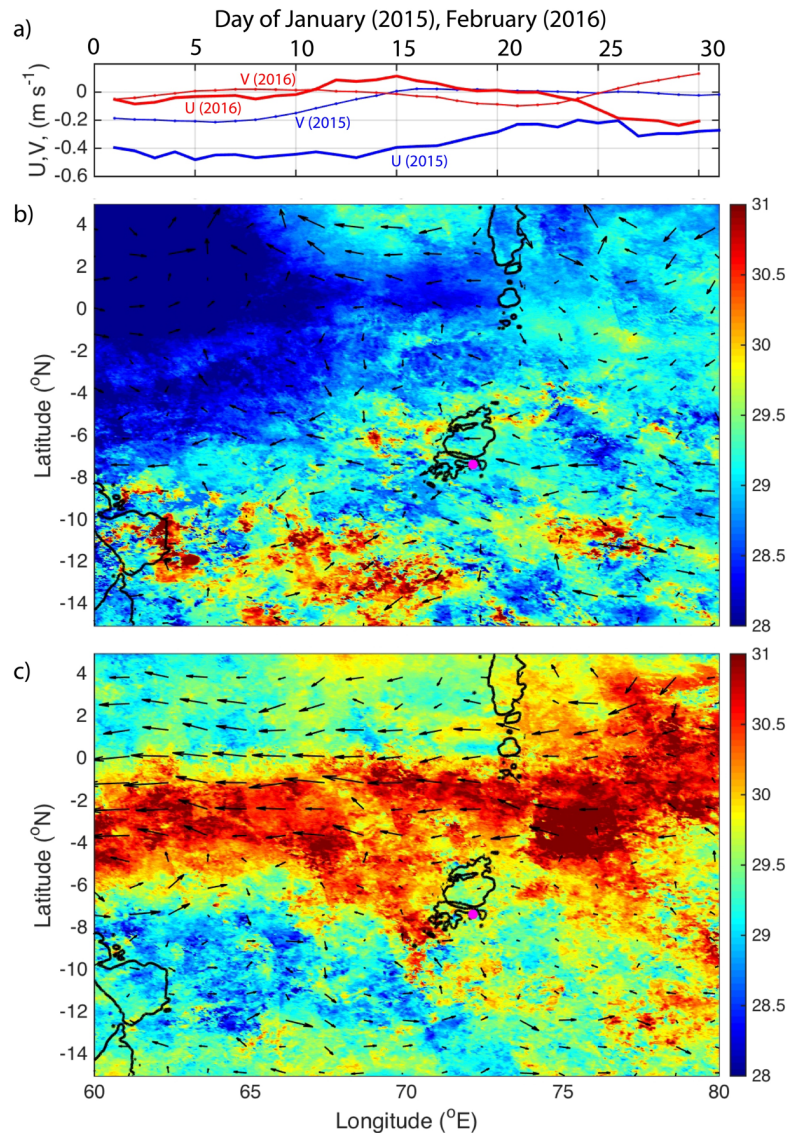
432 The 2015 cruise followed a period during which the MJO was in a strongly positive
433 phase, driving strong and persistent westerly winds over a broad area spanning the
434 equator. Due to the extension of the Seychelles-Chagos Thermocline Ridge (SCTR)
435 within which the thermocline shoals due to Ekman pumping, SST was significantly
436 lower (28°C) to the north-west (Figure 5b) but was also lower more generally
437 throughout the region during 2015 compared to 2016. This was likely due to the
438 turbulent entrainment of cold water from beneath the shallow thermocline due to the
439 enhanced wind stress (Vialard et al. 2008). The shoaling of the thermocline within
440 the SCTR is important to the regional primary productivity throughout the region
441 (Currie et al. 2013) and was likely partly responsible for a plankton bloom 10 days
442 prior to the 2015 mooring deployment. During 2016, a distinct zonal band of higher
443 SST (>30.5°C) extended across the central Indian Ocean to the north of BIOT (Figure
444 5c), accompanied by an intensification of westward currents along the equator and
445 extending 4° of latitude into each hemisphere, thereby not reaching BIOT.

446
447 The significant difference in forcing between 2015 and 2016 lies in the prevailing
448 geostrophic currents. During 2015, the mooring over Sandes was subjected to a
449 persistent south-westward mean current of >0.4 m s⁻¹, decreasing throughout the
450 cruise to 0.2 m s⁻¹ and becoming purely westward (Figure 5a). In contrast, the
451 background geostrophic current during 2016 was <0.1 m s⁻¹ in both components; as
452 a result, the tidal and near inertial currents attain greater significance in the resulting
453 dynamics during 2016 compared to 2015 when the persistent westward current
454 dominated tidal currents.

456 **4.1.2 Tidal, near-inertial and mean current regime**

457 The frequent lack of scatterers in the lower 30 m at the Sandes mooring in 2015
458 precluded accurate estimates of tidal velocities there; as the two mooring locations
459 were so close, we focus on the characteristics of the diurnal and semidiurnal tidal
460 motions over the summit of Swart. Currents exhibited a mixed tidal regime. M₂
461 currents were ~8 ± 2 cm s⁻¹ and directed towards the east-north-east with mean
462 heading of 65°N and little (<10°) variation with depth. K₁ currents rotate with depth

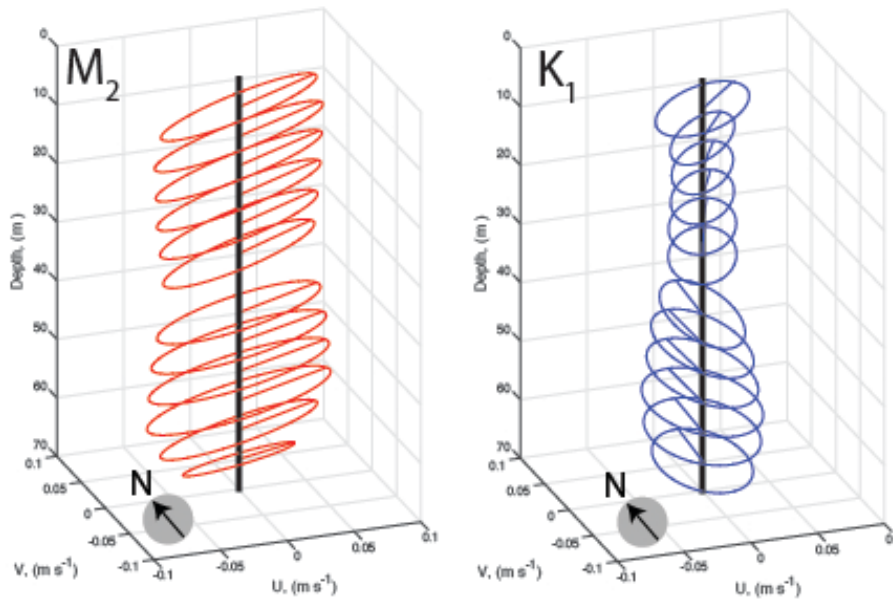
463 from a north east heading at the surface but becoming north west near the bed.
 464 Compared to the semidiurnal tide, amplitudes of the diurnal tide are ~60% of M_2
 465 towards the surface but increase to ~80% at 5 m above the bed (Figure 6).
 466



467
 468 *Figure 5. a) Geostrophic currents during 2015 (blue lines) and 2016 (red lines) at the position of Sandes and Swart as*
 469 *indicated in b) and c) by the magenta dot, and b) sea surface temperature ($^{\circ}C$) and geostrophic velocity vectors during 2015*
 470 *and c) 2016. The 1000 m isobath is indicated by the black contours. SST are monthly means for (2015) January and (2016)*
 471 *February. Geostrophic velocities plotted as vectors in b) and c) are daily values for mid-way through the mooring*
 472 *deployment in each year.*

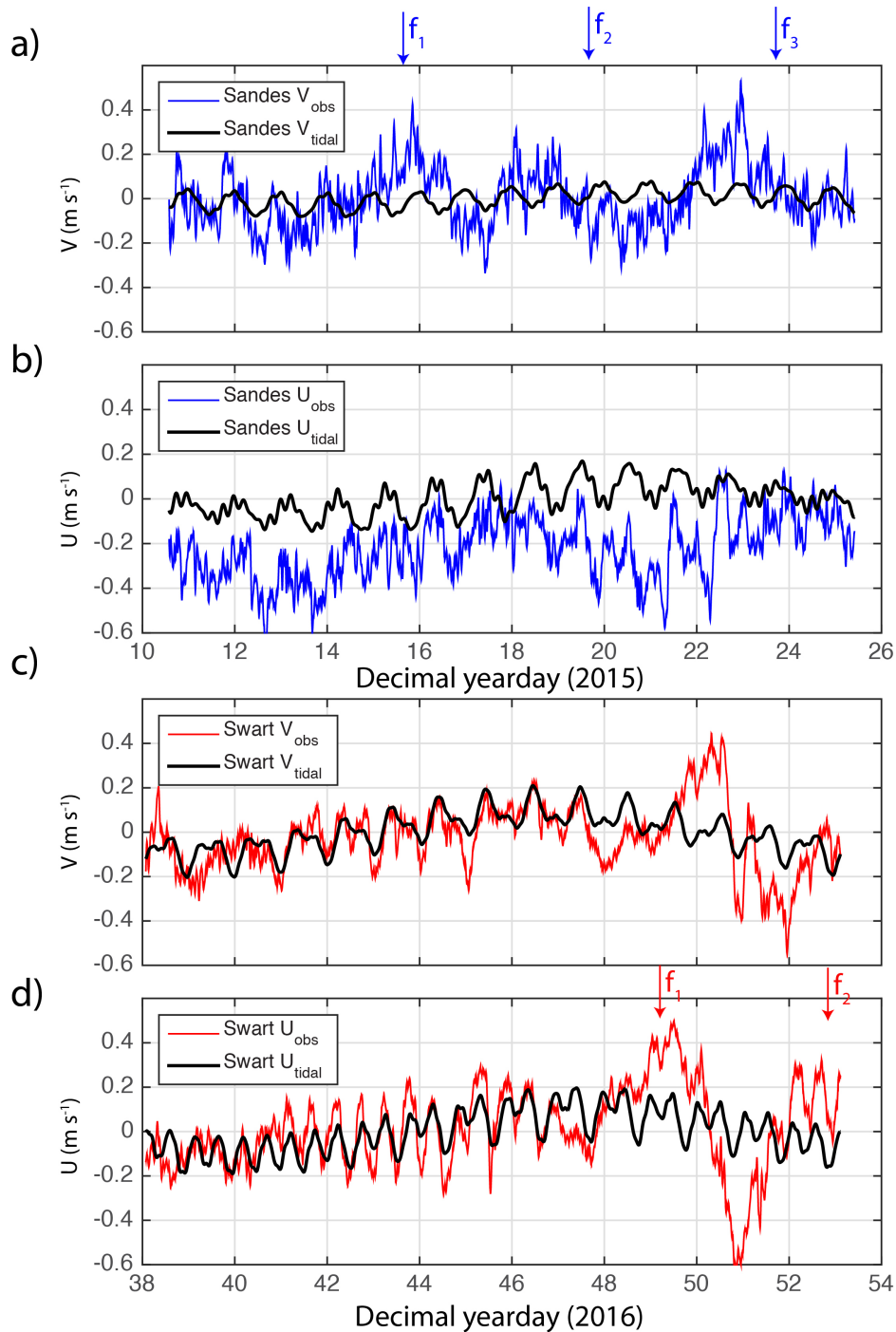
473 The two mooring deployments reflect the potentially strong influence of background
 474 conditions that may influence internal wave generation; during 2015 a steady,
 475 persistent westward current exceeded any eastward tidal current throughout almost
 476 the entire deployment (Figure 7b). The westward current, with typical current speeds

477 of $\sim 0.4 \text{ m s}^{-1}$, was due to a narrow band of elevated westward currents that occupied
 478 the zonal band centred exactly on the mooring location (Figure 5b). Whilst limited in
 479 meridional extent, the current persisted throughout January 2015 although
 480 weakened to 0.2 m s^{-1} by the end of the month. In contrast, geostrophic currents
 481 were weak throughout BIOT during the 2016 cruise, remaining $<0.1 \text{ m s}^{-1}$ throughout
 482 February 2016.
 483



484
 485 *Figure 6. Tidal ellipses for the M_2 and K_1 tidal constituents plotted at 5 m vertical intervals over the summit of Swart during*
 486 *2016 (right).*

487
 488 Observed currents also differed from tidal velocities due to the generation of near
 489 inertial waves by storms that passed the mooring site on day 14 in 2015 and day 48
 490 in 2016. At this latitude (7°S) near-inertial waves have a period of 4.1 days, a
 491 periodicity reflected by the peaks of northward velocity during days 15, 19 and 23 in
 492 2015 (indicated by the blue arrows in Figure 7a) and 49 and 53 in 2016 (red arrows in
 493 Figure 7d). The full depth profile of low-pass filtered currents (not shown)
 494 corroborates the vertical structure of the near-inertial wave as exhibiting upward
 495 phase velocity, indicative of downward energy propagation following the generation
 496 of the wave by strong winds at the sea surface.



497

498 *Figure 7. Observed total (red or blue) eastward (U) and northward (V) currents filtered at 1 cph and predicted tidal currents*

499 *(black lines) at a depth of 50 m at Sandes (a,b) and Swart (c,d). The three blue arrows above a) indicate the periodicity of a*

500 *near inertial wave (period 4.1 days) generated by a storm at the beginning of the cruise, beginning with the peak*

501 *northward velocity towards the end of day 43. Note that the currents appear to suggest the frequency of the wave to be*

502 *superinertial. The two red arrows in d) indicate the peak in eastward velocity associated with a near inertial wave*

503 *generated by the storm on day 48 in 2016.*

504

505 Observed currents at Swart during 2016 were much closer to those predicted by

506 harmonic analysis because of the lack of a background current except when the

507 storm passed BIOT during days 48-50 (Figure 7 c,d). Currents exceeded 0.5 m s^{-1} at t
508 $= 51.0$ and rotated anticlockwise throughout an approximately 4 day period,
509 consistent with the generation of a near-inertial wave. During both 2015 and 2016
510 the near-inertial wave generated currents that rotated with a super-inertial frequency,
511 i.e. a period of slightly less than 4.1 days.

512

513 **4.1.3 Water column vertical structure**

514 CTD profiles acquired adjacent to Sandes and Swart in 2015 and 2016 consistently
515 demonstrated a moderately stratified upper layer above a strongly stratified
516 pycnocline with maximum $N^2 = 3 \times 10^{-3} \text{ s}^{-2}$. The depth of the pycnocline coincided
517 with the depth of the deep chlorophyll maximum (DCM) between 60 and 70 m depth
518 (Figure 8). The layer of maximum chl-a, which consistently approaches $1 \mu\text{g l}^{-1}$
519 throughout the archipelago, has a thickness of approximately 20 m, diminishing to
520 $<0.2 \mu\text{g l}^{-1}$ at a depth of 110 m (Figure 8).

521

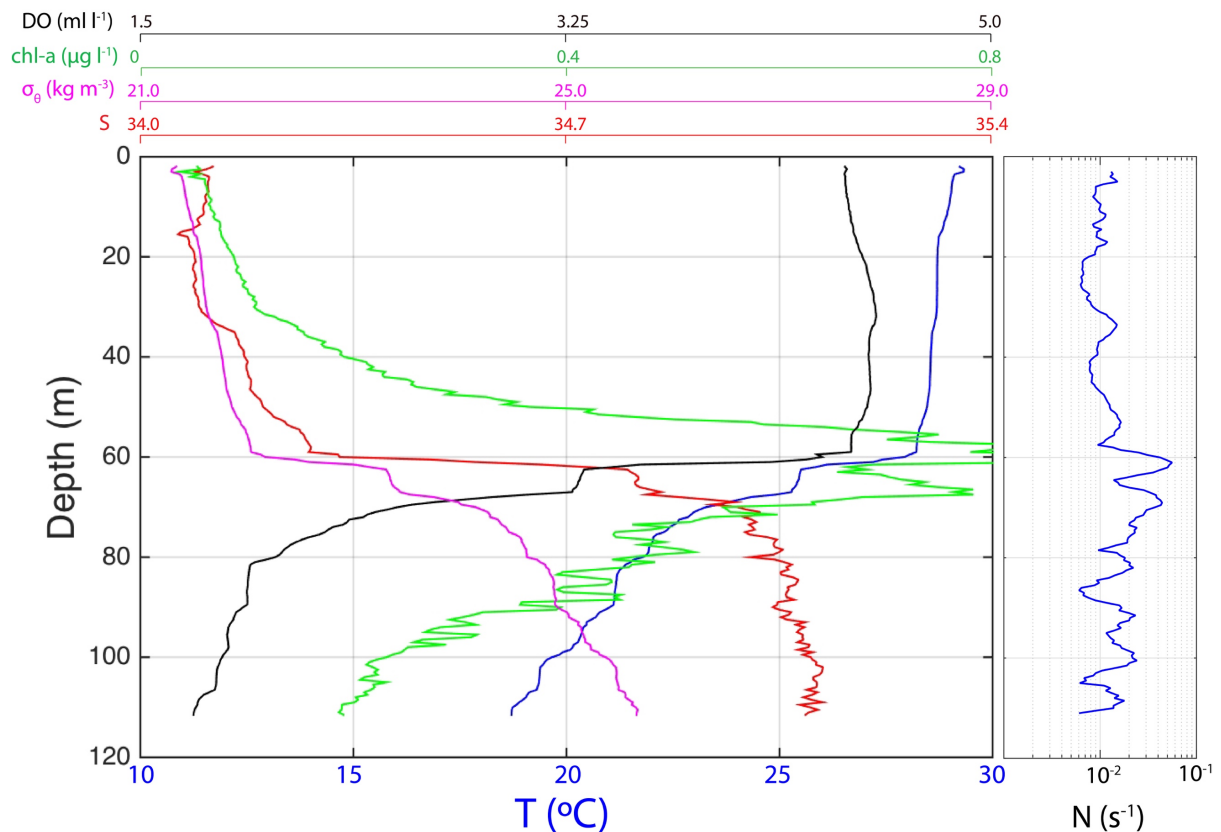
522 At the DCM, dissolved oxygen concentrations decrease rapidly from $>4 \text{ mL L}^{-1}$ to <2
523 mL L^{-1} within 20 m. Thus, the pycnocline at 60 m depth marks the depth of maximum
524 chl-a and lower limit of oxygenated surface waters. It is furthermore a vertical
525 structure that is replicated throughout the archipelago during the 2016 cruise
526 (oxygen was not measured during 2015), although regional scale forcing may
527 influence this, particularly strong wind forcing such as that arising due to the MJO.

528

529 The pycnocline and DCM intersect the seamount summit, such that perturbations in
530 the pycnocline depth will directly drive pronounced changes in water properties over
531 the summit. Most notably, the shoaling of the pycnocline will lead to large reductions
532 in oxygen concentration over the summit. Similarly, the deeper water surrounding,
533 but beneath, the summit is low in dissolved oxygen and contains few phytoplankton,
534 indicating that the zooplankton active during diel vertical migration (DVM) need to
535 reach depths of 60 m or above to benefit from the energy source provided by
536 phytoplankton.

537

538



539
 540 *Figure 8. Vertical profile of temperature (blue), salinity (red), density (pink), chlorophyll-a (green) and dissolved oxygen*
 541 *(black) acquired from a location adjacent to the flank of Swart seamount summit during 2016. The right-hand panel*
 542 *indicates the buoyancy frequency estimated from the corresponding density profile at 0.5 m vertical intervals and following*
 543 *smoothing with a 7 point running average filter.*

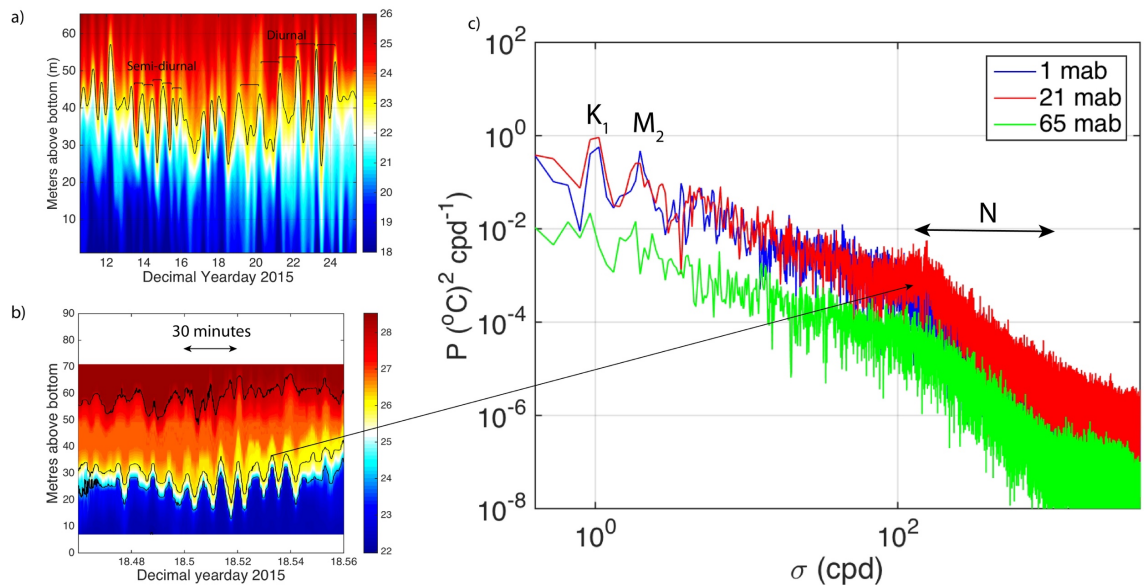
544 **4.2 Internal wave regime: Summit flanks**

545 Given the low latitude of BIOT and the strong stratification, the internal wave band
 546 (IWB) spans a wide range of frequencies in the current study region corresponding
 547 to periods of 4.1 days (i.e. the inertial period) to ~5 minutes. We focus here on the
 548 generation mechanism and implications of isotherm oscillations over the flanks of
 549 Sandes in two frequency bands, tidal and near- N .

550

551 Isotherms oscillate with amplitudes of 20-30 m at both diurnal and semidiurnal
 552 frequencies in the low-pass (3 cycles per day cut off) filtered temperature field (Figure
 553 9a). The temperature variance spectra reflect the comparatively weak stratification
 554 above depths of 40 m (Figure 9c). Variance is more than an order of magnitude less
 555 at 65 metres above bed (mab) than 1 and 21 mab which each have similar levels of
 556 variance that exceed those at 65 mab for all frequencies. Short-period internal waves
 557 appear in packets at Sandes and have periods of ~5 minutes (Figure 9b)

558 corresponding to a distinct increase in variance at $N \sim 200$ cpd at 21 mab (Figure 9c).
 559 where N is the maximum frequency for freely propagating internal waves.
 560



561
 562 *Figure 9. Temperature measured by the mooring deployed over the flank of Sandes during 2015 after filtering a) the entire*
 563 *timeseries at, 3 cpd and b) at 1 minute for a subset of data spanning 1.6 hours. The corresponding variance spectra for*
 564 *heights above the bottom of 1 m, 21 m and 65 m in c) indicate the enhancement at 21 mab at frequencies close to N . The*
 565 *period selected for b) corresponds to the upslope phase of the lee wave where the westward tidal current had relaxed to the*
 566 *extent that the combined impact of the south equatorial current (SEC) and tide on the depression of isotherms on the*
 567 *western flank of the seamount had diminished, enabling the wave to propagate up the slope to the east.*

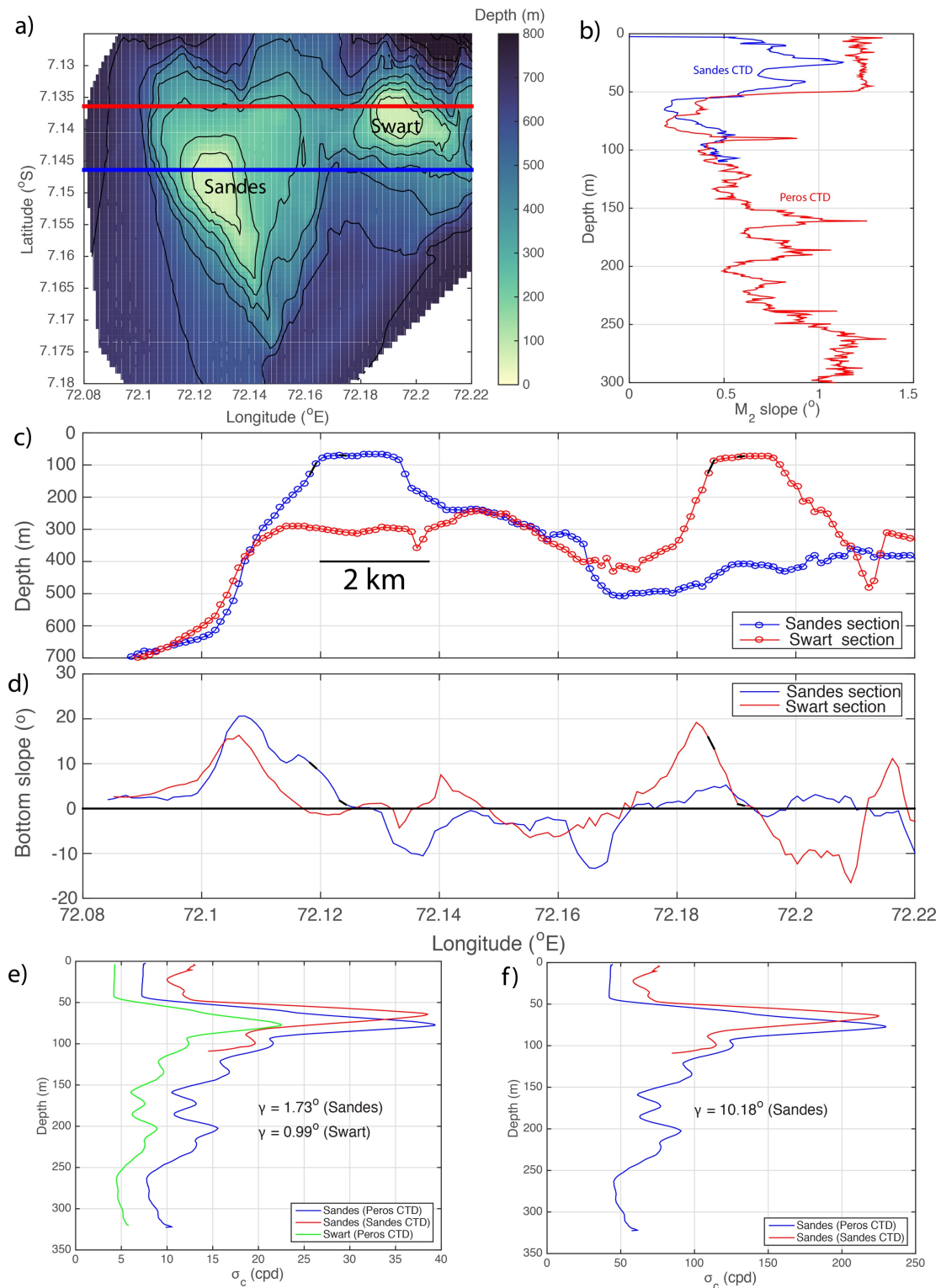
568 **4.2.1 Internal tide: potential generation sites**

569 To evaluate whether internal tides are generated over the sloping sides of the
 570 seamounts and cause the observed isotherm displacements at tidal frequencies, the
 571 wave slope was compared to the bottom slope. Two different CTD profiles were
 572 used to estimate the wave slope; the 2016 profile acquired over the side of Sandes
 573 that reached 120 m and a second profile from Peros Banhos that extended to a
 574 depth of 300 m and enabled an assessment of slope criticality to that depth. The two
 575 profiles were qualitatively similar although the profile from Peros Banhos
 576 demonstrated stronger stratification in the upper 50 m due to more settled
 577 atmospheric forcing at the time of the profile, a property that is not important to the
 578 generation of the internal tide that occurs at or below the depth of the summits at 70
 579 m.
 580

581 The western flanks of Sandes and Swart are similar in terms of the maximum bottom
582 slope, in both cases reaching 20° at depths of 300-400 m. At no location over the
583 flanks do the slopes become less than 5° . As a result, the flanks of the seamount are
584 supercritical to the semidiurnal tide whose slope is $1 - 1.5^\circ$ in the weakest
585 stratification (which increases the steepness of the angle of propagation) and further
586 decreases to 0.25° in the strongest stratification at 70 m depth (Figure 10b). The
587 summits of Sandes and Swart are potentially critical to the M_2 tide but the slopes
588 would need verification with multibeam bathymetry given the small slopes involved
589 that are sensitive to measurement error over short horizontal distances. The bottom
590 slopes on the summits are estimated at the positions indicated by the black lines in
591 Figure 10c, d for Sandes and Swart as 0.73° and 0.99° respectively, rendering them
592 potentially capable of generating internal tides.

593

594 Overall, the slopes associated with Sandes and Swart are, based on observed N
595 profiles, supercritical to all IWB frequencies except for those with frequencies
596 approaching N , the highest permitted for freely propagating internal waves (Figure
597 10e, f). Over the more gentle slopes of the summits, minimum critical frequencies
598 (wave frequencies at which the wave slope matches the bottom slope), are 5 cpd
599 over the summit of Swart and 7-8 cpd over Sandes. The strongest stratification at
600 60-70 m increases the critical frequency to 40 cpd for the weak slopes at the
601 summits but significantly more over the steep slopes below the summit where the
602 Sandes mooring was deployed. Here, critical frequencies reach 225 cpd where the
603 strongest stratification intersects slopes of 10° or more. At this frequency, the wave
604 slope matches that of the bottom and theory predicts elevated shear and turbulent
605 mixing.



606

607

608

609

610

611

612

613

Figure 10. a) Bathymetry over Sandes and Swart with the sections along which depth is presented in c) indicated by the blue and red lines. The wave slope for the M_2 internal tide in b) is estimated using N from 2 CTD profiles, the first adjacent to Sandes (blue line) and the second from Peros Banhos to the north (red line). The bottom slope is presented in d) for both sections indicated in a). The critical frequency for internal wave reflection is calculated for bottom slopes, γ , representative of the summit (e) and the upper slope (f) using the two N profiles used to compute the wave slopes in b). The slope angles are estimated for the locations indicated in c) by the black lines along the sea bed at the upper slope and on the summit of Sandes (blue line) and Swart (red line).

614 **4.2.2 Internal lee wave generation**

615 The supercritical of the slopes suggest that internal lee waves are more likely to be
616 responsible for the isotherm oscillations. Two CTD transects conducted half an M_2
617 tidal cycle apart over the summit of Sandes in 2016 illustrated isotherm displacement
618 consistent with lee wave formation and the subsequent propagation of cold water
619 bores onto the summit (Figure 11). As the measurement period during 2016 lacked
620 the persistent westward flow observed during 2015, the lee wave formation may be
621 expected to be more clearly related to the tidal forcing. Transect 1 followed a period
622 of sustained westward flow due to the near inertial wave which reversed to an
623 eastward flow at $t = 52.0$, approximately 6 hours before the transect (Figure 7d) such
624 that a lee wave generated on the western flank would be able to propagate back up
625 the slope. Thereafter the current is eastward such that eastern flank is in the lee of
626 the prevailing current (Figure 11d).

627

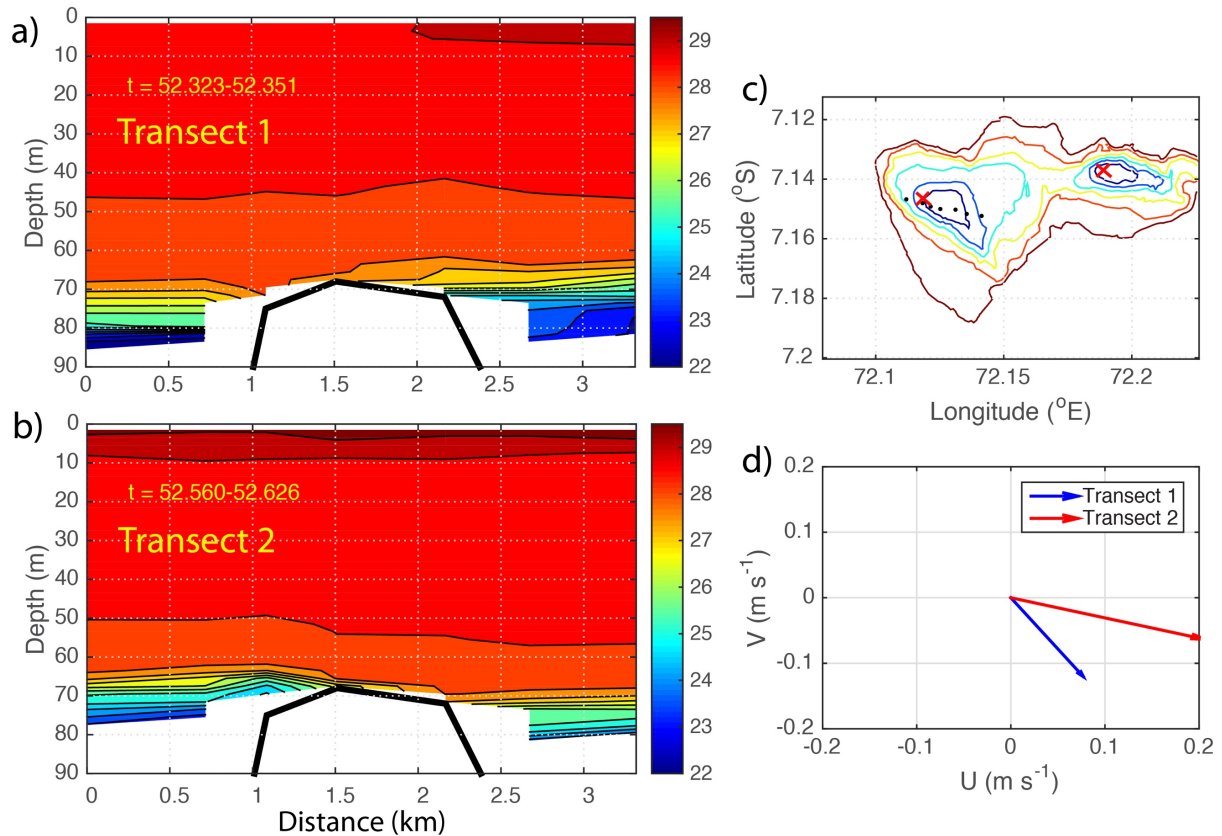
628 The isotherm orientation is consistent with the transition from depressed isotherms
629 on the western flank (left hand side of Figure 11 a,b) to the opposite as the eastward
630 flow intensifies; the cold water on the western flank propagates up the slope between
631 transect 1 and 2 as the current increases in intensity to the east. The lee wave
632 formed by the westward flow was released, allowing the cold water to rebound up
633 the western flank and spill onto the summit. As the eastward velocity increases,
634 isotherms are depressed on the eastern side of the summit as a lee wave is formed
635 on the opposite side of Sandes (Figure 11b). At no time in our observations have we
636 observed any doming of isotherms over the summit consistent with Taylor cap
637 formation.

638

639 The correspondence between isotherm displacement and currents associated with
640 lee wave formation and subsequent propagation as a bottom-trapped bore over the
641 flanks of Sandes is derived from the filtered time series of temperature and velocity
642 measured by the 2015 mooring. The 2015 deployment was characterised by a
643 persistent westward flow; the mooring, located on the western flank, was thus
644 deployed on the downstream (leeward) side of the seamount but the flow was
645 primarily steady with a weaker oscillatory (tidal) component. Consequently, the
646 formation of lee waves is not expected with tidal periodicity (in particular during the

647 first half of the deployment when mean currents were strongest) but rather a
 648 complex function of the total incident current which includes background mean, near
 649 inertial, and tidal currents.

650



651

652 *Figure 11. a),b) Temperature (°C) over Sandes summit (c) during two transects in 2016 that were separated in time by 6*
 653 *hours. The locations of the CTD profiles were indicated in Figure 3 and are again in c) by the black dots. The first station*
 654 *(distance = 0) for both transects was in the west and progressed due east. The heavy black line in a) and b) indicates the*
 655 *bottom depth measured at each location. The time elapsed between the last profile of the first transect (upper panel) and*
 656 *the first profile of the second transect (lower panel) was exactly 5 hours such that the two transects can be considered as*
 657 *having been completed at almost exactly opposite phases of the semidiurnal tide. Due to the influence of the near inertial*
 658 *wave generated 5 days earlier, the total currents measured at the time of each transect indicated in d) are stronger to the*
 659 *south and east than predicted for the tide alone. The red crosses in c) indicate the positions of the 2015 mooring over the*
 660 *flank of Sandes and the 2016 mooring over the summit of Swart.*

661 The near-inertial current in particular, which rotates anticlockwise with a superinertial
 662 period and an amplitude equal to or exceeding the mean geostrophic current,
 663 renders all sides of Sandes as being ‘leeward’ at some stage throughout the ~4
 664 days. As a result, the correlation between the cross-slope currents and isotherm
 665 displacements is not as close as one would expect for ridges considered in previous
 666 studies , e.g. Kaena Ridge, Hawaii (Legg and Klymak 2008; Alford et al. 2014),

667 Luzon Strait (Pinkel et al. 2012; Buijsman et al. 2014) and the Mascarene Ridge (da
668 Silva et al. 2015).

669

670 We therefore focus on the end of the mooring deployment when the zonal
671 geostrophic currents weakened to 0.2 m s^{-1} permitting the tidal currents to exert
672 more influence on the dynamic response over the seamount (Figure 5a). The near
673 inertial wave generated 8-10 days beforehand twice generated meridional velocities
674 that peaked briefly at $>0.4 \text{ m s}^{-1}$ on day 22. By focussing on this period we are able
675 to evaluate the consistency between the orientation of the horizontal currents with
676 the isotherm displacements during a period when the influence of the steady
677 geostrophic current was reduced and tidal motions were more important; for lee
678 waves to be generated we expect the isotherms to be depressed during downslope
679 (south-westward) flow near the bed and for the potentially rapidly rising isotherms to
680 be accompanied by upslope (north-eastward) flow. Vertical structure in the horizontal
681 currents permit an approximate estimate of the vertical wavelength, suggested
682 above to scale as $\pi U_d / N \approx 30 \text{ m}$.

683

684 Consistent with the generation of lee waves by a south-westward flow and
685 subsequent propagation to the north east as the current weakens, we observe 4
686 distinct events during days 22-24 characterised by a rapid decrease in temperature
687 at the bed as cold water moves upslope with semidiurnal frequency (Figure 12). The
688 events are preceded by a gradual deepening of isotherms and downslope flow,
689 indicative of the formation of a lee wave. The thermal structure is replicated further
690 from the bed with downward displacements of the 28°C isotherm of $>20 \text{ m}$
691 amplitude, consistent with the simulations of Klymak et al. (2010a).

692

693 Significant vertical structure is observed in both the cross-slope and along-slope
694 baroclinic velocity components, with each component oscillating in the vertical with a
695 30-40 m wavelength. Currents immediately above the bed are predominantly
696 directed downslope (blue shading in Figure 12 b) until the isotherms rebound; cold
697 water appears near the bed at the same time as near bed currents reverse to an
698 upslope orientation.

699

700 The echo intensity provides a measure of suspended particulate matter but also
701 stratified turbulence. The dominant signal apparent in Figure 12e is the diel vertical
702 migration of zooplankton; echo intensity is higher during night time (between $22.8 < t$
703 < 23.3 and at the same time every day) due to the presence of mesopelagic
704 organisms (e.g. zooplankton and small fish) that had migrated to the upper 100 m
705 from the deep scattering layer which here is at 400 m depth (Letessier et al. 2016).
706 Note that the clear water apparent at $t = 23.0$ occurs during the downslope phase of
707 the lee wave formation. Clear water was observed during the same phase of
708 downslope flow by (van Haren and Gostiaux 2010) over the flanks of Great Meteor
709 Seamount where similar bore-like features were observed and accompanied by high
710 frequency waves with frequencies approaching N .

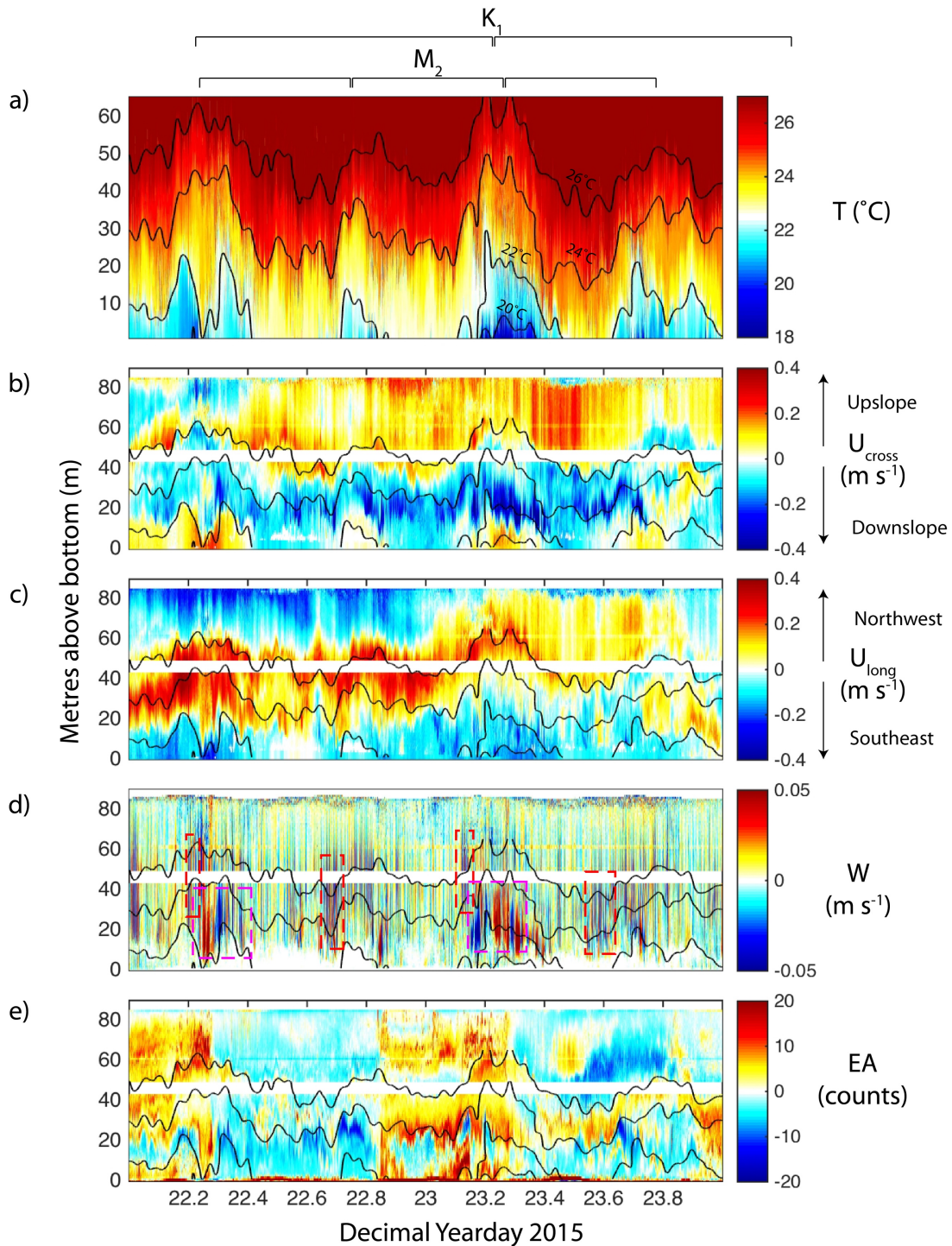
711

712 **4.2.3 High frequency, near N internal waves**

713 Whilst the isotherms oscillate with tidal periodicity and ‘rebound’ vertically with a
714 shock-like leading edge as is typical for propagating internal bores (e.g. Hosegood
715 and van Haren 2004), there are clearly higher frequency oscillations present
716 throughout the record over the flanks of Sandes and which are most intense during
717 the upslope phase of the lee wave. The waves have periods of ~5 minutes and
718 reach amplitudes of 20 m (Figure 9b). This frequency equals that of the maximum
719 value of the local buoyancy frequency, N , observed in the CTD profile over the flank
720 of Sandes at a depth of 60 m (Figure 8) which is furthermore the depth where the
721 high frequency waves are observed (red boxes in Figure 12d). Thus, high frequency
722 internal waves propagate along the thermocline with a frequency centred on the local
723 buoyancy frequency which attains its maximum value at that depth.

724

725 Packets of near- N waves are most pronounced at $t = 22.25$ and 23.25 (identified by
726 the dashed boxes in Figure 12d), indicative of a dominant diurnal tidal component
727 during the period presented here. A detailed view of such waves was presented in
728 Figure 9b. However, weaker signals are also evident at semidiurnal frequency, i.e. $t =$
729 22.75 and 23.75 . The vertical velocity, W , is enhanced at two different frequencies;
730 at mid-depth on the leading edge of the bore (red dashed boxes in Figure 12d) the
731 characteristic signature of nonlinear internal waves is observed as an alternating



732

733

734

735

736

737

738

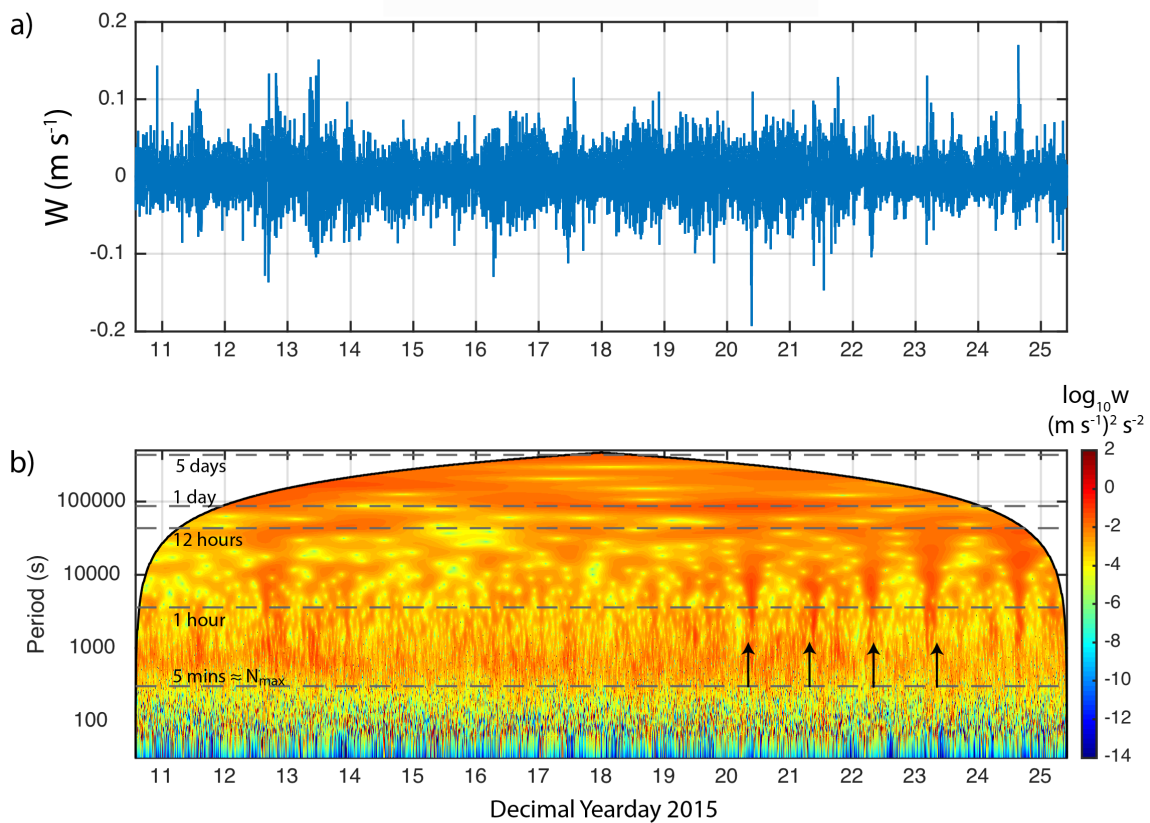
739

740

741

Figure 12. a) Temperature, baroclinic b) cross-slope and c) long-slope velocities, d) vertical velocity and e) echo amplitude anomaly measured by moored ADCPs over the flank of Sandes during 2015. Velocity data are filtered at 1 cycle per hour. The echo anomaly is computed as the measured return signal strength intensity with the time mean for each depth bin subtracted. The dashed boxes in d) times during which different internal wave frequencies were dominant; red boxes indicate high frequency (near N) wave packets as exemplified by Figure 9b) and the pink boxes slower wave motions associated with the bore's passage upslope. The horizontal lines at the top of the figure indicate the periods associated with the semidiurnal (M_2) tidal constituent and the diurnal (K_1) constituent. Note that the colour shading in a) corresponds to the unfiltered (10 second) temperature data but the isotherms presented as black contours in each panel are the temperature filtered at 1 cycle per hour to remove high frequency content.

742 band of upwards and downwards velocities corresponding to isotherm displacements
 743 with periods $O(10 \text{ minutes})$ that represent the near- N waves. The occurrence of
 744 these wave groups with tidal periodicity is apparent in the wavelet scalogram at 60 m
 745 depth (30 mab) of the vertical velocity component. Elevated variance is seen to
 746 extend from tidal frequencies down to N with a corresponding period of 5 minutes
 747 (Figure 13). Following this wave packet, a more sustained pattern of downward
 748 velocity is associated with the deepening of the 22°C isotherm and then a sustained
 749 upward velocity as the isotherms rapidly shoal (pink dashed boxes in Figure 12d).
 750 The latter corresponds to the upslope passage of the bore that evolved from the lee
 751 wave.



752
 753 *Figure 13 a) Vertical velocity measured at 60 m depth (30 mab) and b) the corresponding wavelet scalogram for the*
 754 *mooring deployment over the flank of Sandes, 2015. The horizontal grey dashed lines in b) represent periods ranging from*
 755 *the maximum local buoyancy period, $N_{\max} = 5 \text{ minutes}$, to 5 days. The vertical black arrows between days 20 and 24*
 756 *indicate the occurrence of high frequency wave packets within which waves with periods reach N_{\max} with a diurnal*
 757 *periodicity. Note the rapid diminishment of energy at periods less than N_{\max} , demonstrating the limiting frequency of N for*
 758 *internal waves.*

759
 760

761 **4.3 Summit flushing events by propagating internal bores**

762 The previous section demonstrated that, during 2015 when background mean
763 currents were significant in comparison to the tidal currents, internal lee waves
764 formed on the western flank of Sandes. With a weakening of the prevailing current,
765 the lee waves evolved into hydraulic jumps and propagated up the slope as internal
766 bores, accompanied by high frequency internal wave packets, with tidal periodicity.
767 In this section, we demonstrate that these bores reach the summit and flush the bed
768 with cold water originating from depths below that of the summit. We first present the
769 whole time series from the summit of Swart in 2016 to demonstrate the persistence
770 of the bore propagation before focussing in detail on one event to highlight the
771 dynamics and implications.

772

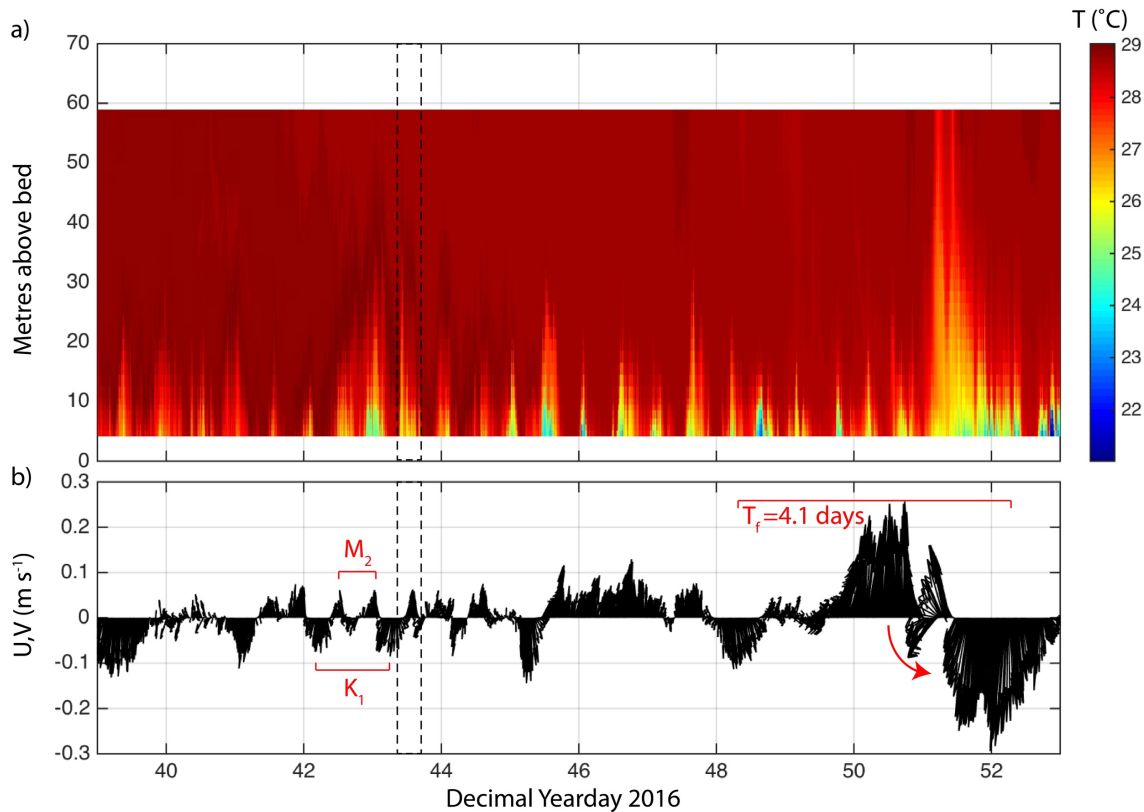
773 **4.3.1 Bore periodicity: tidal dominance**

774 As a result of the tidal dominance of the hydrodynamic forcing, the bottom-trapped
775 bores appeared with a predominantly semidiurnal periodicity (Figure 14a). Their
776 vertical extent was usually <30 m but the cold water signature extended towards the
777 surface following the storm after day 50, presumably due to elevated mixing. The
778 coldest temperatures observed near the bed most often coincide with the periods
779 immediately following more sustained southward flow (for example on days 45, 48)
780 that are associated with the diurnal tide (see annotation indicating diurnal period in
781 Figure 14b).

782

783 The temperature signal associated with the bores was most pronounced along the
784 pycnocline that, whilst on average was observed at a depth between 60-70 m, varied
785 in vertical position with the passage of the bores due to the elevation of isopycnals
786 by individual waves. The vertical velocity associated with the nonlinear waves carried
787 a signal over the water column that, when viewed in frequency space, highlights the
788 frequency range within which the waves exist. Energy spectra for vertical velocity
789 exhibit a broad-band enhancement for $30 < \sigma < 300$ cpd, similar to the high
790 frequency (i.e. near- N) waves observed over the flanks of Sandes (Figure 15). To
791 examine in more detail the structure and properties of an individual bore, we focus
792 on the period $t = 43.6 - 43.75$ indicated by the dashed black box in Figure 14.

793



794

795 *Figure 14. a) Temperature and b) geostrophic (depth mean) velocity over the summit of Swart during 2016. The dashed*
 796 *black box indicates the period for which detailed observations are presented below. The principal timescales of variability*
 797 *are indicated in b) as the near inertial period, T_f , at which currents rotate counter-clockwise (indicated by the red arrow)*
 798 *with a period of 4.1 days following storm forcing at the surface, the semidiurnal tide (M_2) and diurnal tide (K_1).*

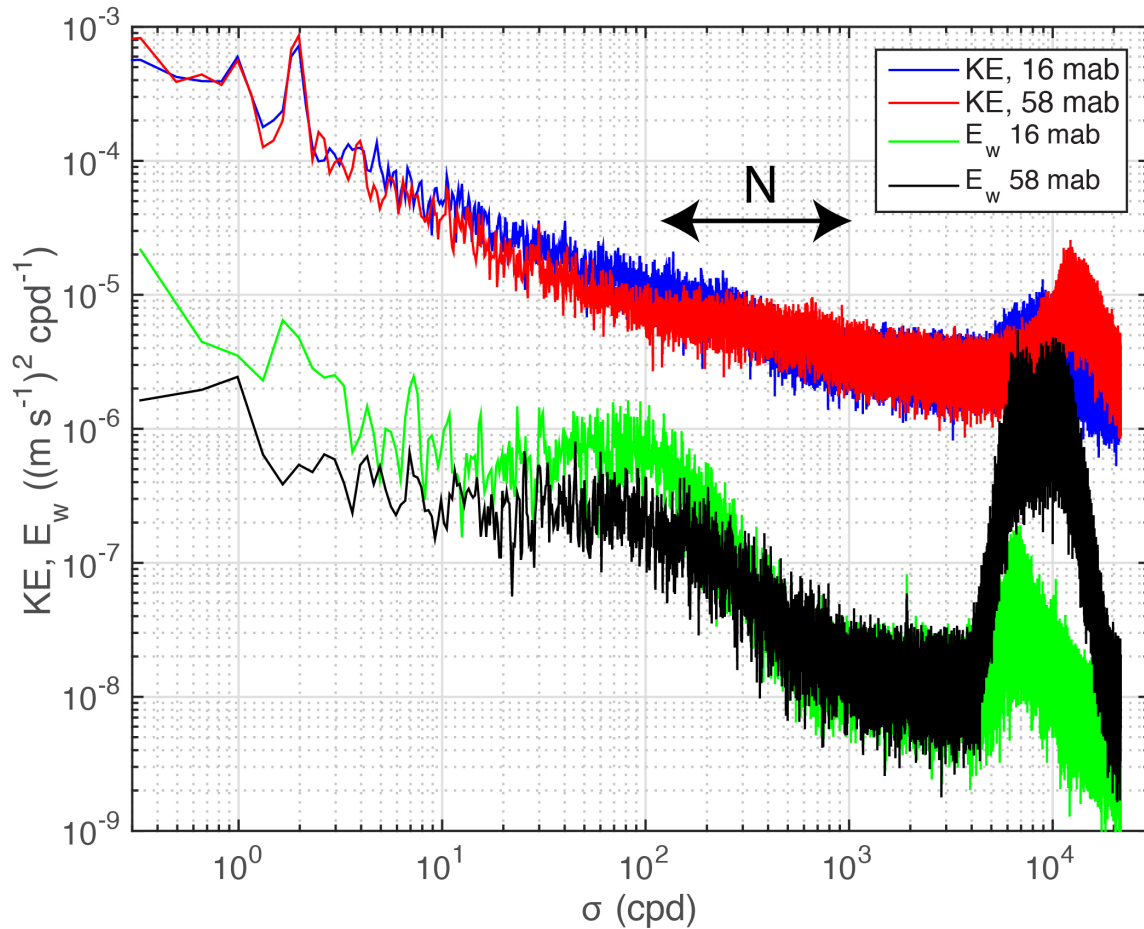
799 **4.3.2 Bore characteristics and implications for mixing**

800 The bore passing the mooring at $t = 43.6$ is representative of the bores that
 801 propagated over the summit with every semidiurnal tide. For layer heights and
 802 densities of 20 m, 1024 kg m^{-3} (lower) and 50 m, 1021 kg m^{-3} (upper), we find $c_{\text{linear}} =$
 803 0.65 m s^{-1} , which is approximately double the typical maximum particle velocities of
 804 0.3 m s^{-1} and therefore defines the event as a bore.

805

806 Based on the particle velocities beneath the 28°C isotherm, the bores propagate to
 807 the north-east, consistent with their generation by the lee wave formed during the
 808 previous tidal cycle, (i.e. $43.1 < t < 43.6$) when the barotropic flow was directed to the
 809 south west (black vectors in Figure 16a); as the tide reversed, the wave evolved into a
 810 bore that propagated onto the summit to the north east. The bore in this instance
 811 contains water with temperatures of $\sim 25^\circ\text{C}$ which, on the basis of the CTD profile
 812 presented in Figure 8, suggests the source water to be only just below the summit

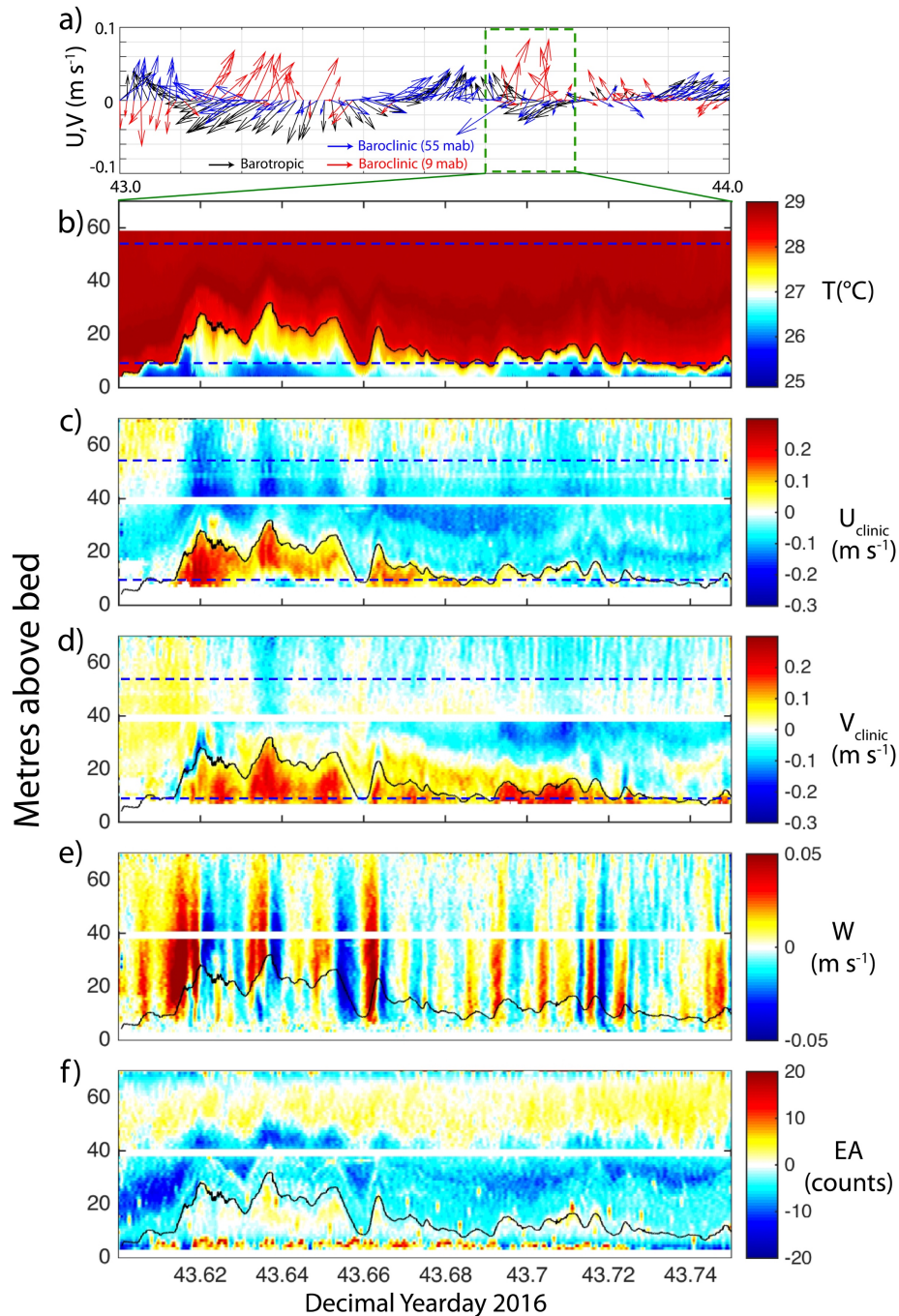
813 depth. At other times during the mooring deployment, temperatures reach $<22^{\circ}\text{C}$,
 814 suggesting the bores to have originated at depths >90 m, 20 m below the depth of
 815 the summit.



816
 817 *Figure 15. Energy spectrum for kinetic energy (KE) and vertical velocity measured at 16 and 58 mab by the ADCPs moored*
 818 *over the summit of Swart during 2016. The broadband enhancement in the vertical velocity component at $30 < \sigma < 300$ cpd*
 819 *at 16 m above the bed represents the signature of the high frequency waves accompanying the bores. The larger peak in*
 820 *energy towards 10^4 cpd represent surface waves with typical periods of 8 seconds.*

821 A sharp leading edge to the bore exhibits a 2°C decrease in temperature within 75
 822 seconds and was accompanied by the characteristic ‘rotor’ of vertical velocity, with
 823 strong upward vertical velocity of $O(10 \text{ cm s}^{-1})$ at $t = 43.615$ followed immediately by
 824 comparable downwards vertical velocity. The individual waveforms that follow the
 825 initial front each exhibit a similar vertical velocity signature and have periods of ~ 5
 826 minutes, thereby having the same near- N frequency as the waves observed over the
 827 flank of Sandes.

828



829

830 *Figure 16. Detailed observations of a bore over the summit of Swart during 2016 at the time indicated by the dashed black*
 831 *box in Figure 14; a) barotropic and baroclinic velocities during the time of the bore and the period beforehand ($t = 43-44$)*
 832 *when the lee wave was generated by the south westward tidal flow between $43.0 < t < 43.5$, b) temperature during the*
 833 *bore and the associated baroclinic c) eastward and d) northward velocities, the e) vertical velocity and f) echo anomaly. The*
 834 *black contour in d)-f) represent the 28°C isotherm and the blue horizontal dashed lines in c) and d) the depths for which the*
 835 *baroclinic velocities are plotted in a).*

836 The bore presented here occurred towards the end of daytime when the echo
 837 intensity was low due to a lack of scatterers in the water column except for a 20 m
 838 thick layer towards the surface that was always present during the day (Figure 16f).

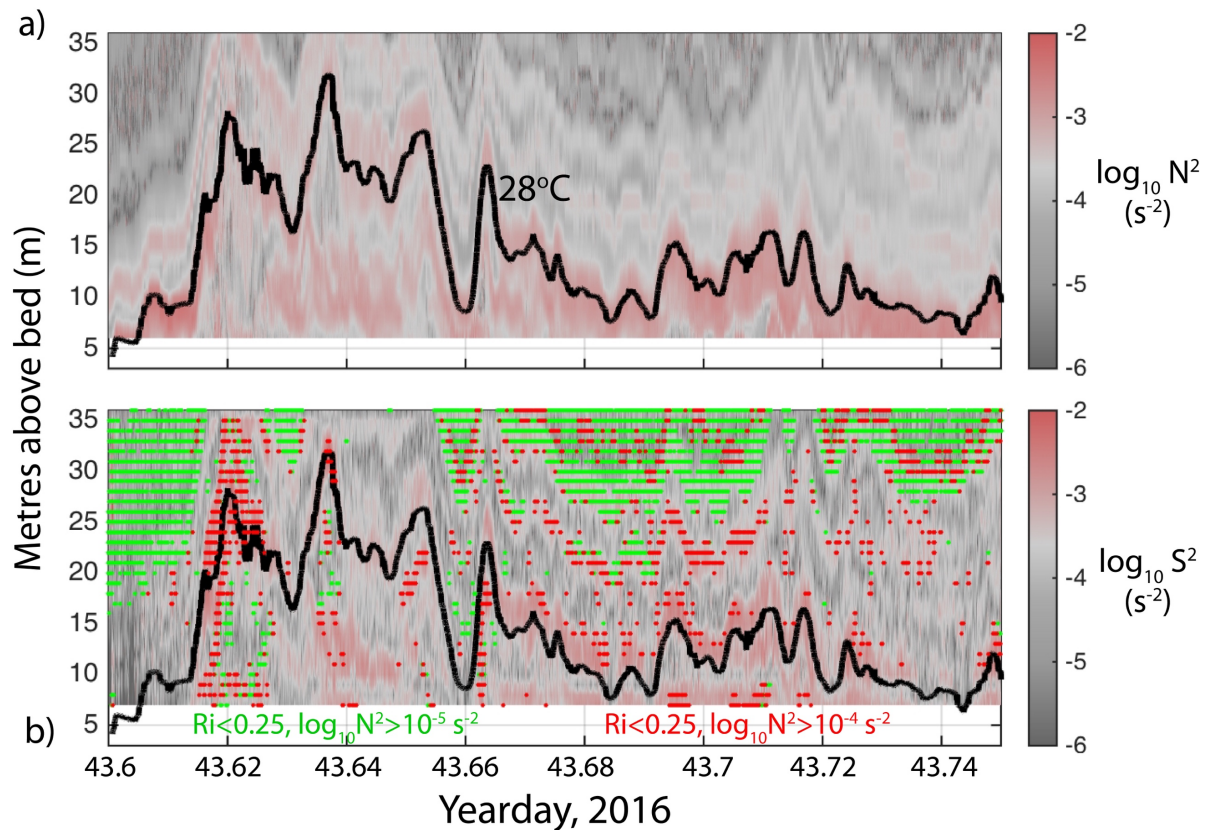
839 Otherwise, the echo intensity displayed the expected diurnal signature of high echo
840 intensity during night-time when the organisms from the deep scattering layer
841 migrated to the upper 100 m. It is nonetheless notable that the bores are always
842 associated with particularly clear water but that the echo intensity is increased within
843 the cold water beneath the 28 °C isotherm. We do not know at present whether the
844 increase is due to resuspended particles, which would be expected in the presence
845 of such strong vertical velocities, or stratified turbulence that may arise from shear
846 instability.

847

848 Horizontal velocity is strongly sheared in the vertical; the cold water within the bore
849 propagates to the northeast but is overlain by baroclinic velocities directed to the
850 southwest. The interface between the two layers is thin, <5 m in vertical extent and
851 corresponds to the position of the 28°C isotherm (indicated by the black contours in
852 Figure 16).

853

854 Both shear and stratification are enhanced within discrete layers of vertical extent <5
855 m (Figure 17) but which are not co-located. Instead it is the shear layers that
856 decrease Ri to critical values of <0.25, indicated in Figure 17b as coloured dots. An
857 example can be found immediately above the 28°C isotherm in Figure 17; the depths
858 immediately surrounding the isotherm are strongly stratified, i.e. $N^2 > 10^{-3} \text{ s}^{-2}$, but the
859 layer immediately above, separated by only 5 m, exhibits diminished stratification but
860 elevated shear. It is these layers in which shear instability is likely to occur and lead
861 to the generation of Kelvin-Helmholtz (K-H) billows that may be the highest
862 frequency waves we observe accompanying the bores. We note that the short
863 vertical distance over which layers of enhanced stratification (~10 m) are observed
864 likely limits the vertical scale to which the billows grow. We do not have direct
865 estimates of turbulence but examined the vertical profiles of temperature to identify
866 any overturns that are indicative of turbulence. Surprisingly none were found despite
867 such bores being typically characterised by energetic turbulence. Except for the
868 leading wave in the bore, patches of low Ri are typically 2 m in vertical thickness,
869 which is the minimum vertical spacing of temperature sensors; thus is entirely
870 feasible that we did not resolve active overturns that were constrained by the vertical
871 scale of the stratification to thin layers of <2 m thickness.



872

873 *Figure 17. a) Buoyancy frequency squared, N^2 (derived from temperature only) and b) shear squared, S^2 during the passage*
 874 *of the bore described in Figure 16. The black line in a, b, represent the position of the 28 °C isotherm. The red and green dots*
 875 *in b) indicate locations where the $Ri < 0.25$, with green dots indicating those regions in which $N^2 > 10^{-5} \text{ s}^{-2}$ and red dots*
 876 *where $N^2 > 10^{-4} \text{ s}^{-2}$.*

877 **5. Discussion**

878

879 Our results suggest that the dynamic, energetic internal wave events observed over
 880 and adjacent to the seamount summits may be important to local ecology as
 881 compared to more slowly evolving processes such as Taylor caps that are invoked
 882 as a mechanism explaining enhanced productivity over seamounts (e.g. Genin
 883 (2004). The formation of lee waves and their transition into internal bores (
 884 Figure 4) supports the theoretical results of Chapman and Haidvogel (1992) who
 885 suggest the internal lee waves over a tall, isolated seamount destroy the fluid
 886 trapping of a Taylor cap. In the present case, there is no evidence of isopycnal
 887 doming nor of fluid retention; whilst more extensive surveys would be required to
 888 conclusively demonstrate this to be the case, the clear evidence demonstrating the
 889 persistent generation of lee waves over the flanks of Sandes and Swart, and their
 890 subsequent propagation as internal bores onto the summits renders it highly unlikely

891 that Taylor caps would be able to persist in the presence of such energetic internal
892 waves.

893

894 The bore occurrence and intensity is impacted by the combination of barotropic tidal
895 forcing and mean current, the latter of which is determined by the relative position of
896 the south equatorial current (SEC) and basin-scale variability due to, for example,
897 the MJO. This is consistent with the numerical modelling of da Silva et al. (2015) who
898 found that the internal wave generation over the Mascarene Plateau in the Indian
899 Ocean was sensitive to the superposition of the barotropic tidal forcing and the
900 properties of the SEC that varied over time. In the present case, this implies that the
901 modulation of the background mean current due to instabilities in the SEC and other
902 regional/basin-scale flow fields hold the potential to modify the biophysical regime
903 around and on top of the seamounts. Taken in combination with the influence of the
904 MJO on regional scale productivity, it is clear that any assessment of the influence of
905 such dynamic features on the biological environment require a careful and thorough
906 understanding of the wider dynamical system to place observations that are
907 potentially sparse in a temporal sense into the correct context. The key role played
908 by tidal forcing in our results and the properties of the highly sheared bores
909 described above reinforce the findings of Turnewitsch et al. (2016) who determine
910 tidally generated internal waves at a tall seamount 1) promote the sudden injection of
911 nutrients to the euphotic zone and subsequent increase in primary production and 2)
912 increase settling rates of resuspended particles by the shear-driven aggregation of
913 smaller, slower-settling particles.

914

915 Whilst our observations are qualitatively consistent with the results of numerical
916 simulations of lee waves generated over similar topography, we note that three-
917 dimensionality is inevitably important over Sandes and Swart. For example, the near-
918 inertial wave during 2015 significantly increased meridional velocities, thereby
919 rendering the northern and southern sides of the seamounts subject to lee wave
920 generation rather than the eastern and western flanks as would be the case when
921 the tide is superimposed on a predominantly zonal mean flow. Future numerical
922 simulations for the current configuration may shed light on the preferred locations of
923 lee wave formation but the simpler current regime during 2016 demonstrates that the
924 tide alone is effective at generating bores over the western flanks that then

925 propagate to the north east with the turning of the tide. The almost circular nature of
926 the summits here render significant portions of the summit flanks susceptible to the
927 direct impact of lee wave formation and internal bore propagation; as the region of
928 most intense activity is the transition from steeply sloping flanks to the flat summit,
929 we therefore note the close correspondence between the local dynamics and
930 preferred habitat for the silvertip shark population consistently observed over the
931 upper flanks of the seamounts.

932

933 The undular structure of the bore is consistent with bores observed elsewhere and in
934 a range of conditions and geophysical settings, for example the 30 m-high 'solibores'
935 observed at 500 m depth in the Faeroe-Shetland Channel (Hosegood and van Haren
936 2004) but also the 'solitary-like wave features' on the shelf inshore of Monterey Bay,
937 where the waves had the same amplitude (20-30 m) in approximately the same
938 water depth (80 m) as observed here (Carter and Gregg, 2002). The bores here
939 were accompanied by packets of high frequency (near- N) waves. Whilst the waves
940 were observed near a sloping bed and had frequencies near to N that were
941 furthermore close to the critical frequency, we propose that they were *not* indicative
942 of critically reflecting incident internal waves but due to local generation by shear
943 instability. Enhancement of vertical displacement spectra at the critical frequency
944 was observed over the bed of Fieberling Guyot and attributed to reflection of a
945 broadband incident internal wave field; the critical frequency was close to the local
946 buoyancy frequency but, due to weaker stratification, approximately an order of
947 magnitude lower than that observed here (Eriksen 1998). The 'near- N ' waves here
948 are instead trapped within a narrow waveguide, i.e. the thermocline that oscillates
949 with the lee wave formation and subsequent propagation as an internal bore. Similar
950 waves were observed in the North Sea shelf sea environment where they may
951 contribute to nutrient input to surface layers (Van Haren 2005). In the present case,
952 the amplitude of the high frequency waves is remarkably consistent with the findings
953 in the North Sea where the maximum amplitude equalled half the vertical scale of the
954 mean pycnocline; the typical amplitude is 10 m but reaches a maximum of 20 m
955 here, all within a thermocline of 20-40 m vertical scale.

956

957 The origin of the near- N waves may be through shear instability. Despite little
958 evidence of overturns, low Richardson numbers indicate a highly-sheared

959 environment conducive to shear instability. The waves in our observations are very
960 similar in period, $O(1$ minute), amplitude (10 m) and associated properties as the
961 Kelvin–Helmoltz (K-H) billows, which are generated by strongly sheared flows,
962 observed over the flanks of the larger Great Meteor Seamount (van Haren and
963 Gostiaux 2010). The K-H billows were observed to have anomalously high echo
964 intensity due to their timing of occurrence coinciding with clear water during
965 downslope flow; their turbulent nature rather than particulate matter increased the
966 acoustic reflectivity. In our observations, we also note that the high frequency wave
967 trains occur during periods of low acoustic reflectivity, indicative of clear water, but
968 instead of occurring during downslope flow, our wave trains occur during upslope
969 flow as the bores propagate towards the summit although this event follows a period
970 of sustained downslope flow. The generation of high frequency waves that may
971 represent K-H billows is consistent with the laboratory and numerical results of
972 Cabeza et al. (2009) that show K-H billows to develop as secondary instabilities of a
973 highly sheared lee wave developed over an abrupt obstacle. Their results highlighted
974 the importance of abrupt topographies in developing hydraulic control points at lower
975 Froude numbers than more rounded obstacles. We propose that the ubiquity of the
976 near- N waves in our observations is a direct result of the sharpness of the transition
977 for summit to slope over Sandes and Swart that renders the downstream flank
978 permanently supercritical and the interface critical to shear instability.

979

980 Whilst the isotherm oscillations considered here are consistent in all ways with lee
981 wave generation, we are unable to diagnose the role of incident internal (tidal) waves
982 generated remotely by baroclinic lee waves (Stashchuk et al. 2007). Given the
983 ubiquity of steep topography throughout BIOT, it is highly likely that that lee wave
984 generation is an ubiquitous feature throughout the archipelago and which can radiate
985 away as linear internal waves. Johnston & Merrifield (2003) consider the refraction
986 and reflection of incident mode 1 internal waves on ridges and seamounts and
987 demonstrate that, for supercritical slopes as considered here, horizontal refraction
988 leads to an alternating band of low and high energy density in the lee of ridges. Over
989 sloping topography, higher modes which are more susceptible to local dissipation,
990 develop to maintain the mode-1-like structure, elevating vertical shear over
991 topography. In the case of an isolated seamount such as Sandes or Swart, flow due

992 to an incident mode-1 wave may be diverted around rather than over the seamount,
993 inhibiting scattering when compared to a ridge.

994

995 We are unable to definitively link the aggregation of the dense silvertip shark
996 population to the lee wave generation but we note the qualitative consistency with
997 other locations where resident shark populations exhibit a strong preference in their
998 choice of location around isolated topographic features. At El Bajo Espiritu Santo, an
999 isolated seamount in the Gulf of California, large polarized schools of adult scalloped
1000 hammerheads were observed to remain along the drop off into deep water but to
1001 also migrate with diurnal frequency up to 8 km away from the slope before returning
1002 in rhythmical fashion (Klimley and Nelson 1984). The location of the shark
1003 aggregation corresponds to the lee side of the seamount with respect to the tidal
1004 currents. The seamount sides appear to be highly supercritical, indicating that
1005 environment to be conducive to the formation of internal lee waves, just as we
1006 observe here. The same scenario appears to occur in the Galapagos but the lack of
1007 current measurements in Hearn et al. (2010) prohibit an assessment of the
1008 consistency between the aggregation of hammerheads on the eastern flank and the
1009 location of lee wave formation. Whilst beyond the scope of the present work, we
1010 consider that the turbulent flow field in the region of lee wave generation increases
1011 the schooling of the forage fish known to be abundant over the seamounts (Liao,
1012 2007). Previous observations over a submarine Bank in the Celtic Sea demonstrated
1013 an increase in schooling, and subsequently foraging by predators, at times of internal
1014 wave propagation (Embling et al. 2013). Schooling fish conserve energy in a
1015 turbulent flow (Alexander 2004) in addition to reducing predation by predator
1016 confusion (Olson et al. 2012); however, schooling also exposes the weaker
1017 individuals who are unable to maintain their position in the school, leading to an
1018 overall increase in predation success rates (see Thiebault et al. (2016) for a review).

1019

1020 **6. Summary**

1021

1022 Observations made primarily with a taut-line, subsurface oceanographic mooring
1023 deployed during two consecutive years over, firstly, the flanks of Sandes seamount
1024 in the Chagos archipelago during 2015 and, during the following year of 2016, the
1025 summit of a physical identical neighbouring seamount, Swart, demonstrate the

1026 generation of internal lee waves. The waves, which had amplitudes of 20-30 m,
1027 formed in response to the prevailing currents that comprised to varying degrees a
1028 combination of mean background geostrophic, near inertial, and tidal currents. The
1029 steepness of the seamount sloping sides, which were strongly supercritical to the
1030 internal tide at both diurnal and semidiurnal frequencies, and the rapid transition from
1031 the flat summits promoted conditions within which the lee waves transformed into
1032 hydraulic jumps. As the forcing relaxed, the jumps propagated up the slopes as
1033 bottom-trapped internal bores. The bores were accompanied by packets of short
1034 period internal waves whose frequencies approached that of the local buoyancy
1035 frequency and were furthermore at the critical frequency for internal wave reflection.

1036

1037 The observations made over the seamount summit revealed that bores continued
1038 onto flat summits with tidal periodicity during the second year (2016) when the
1039 currents were predominantly tidal. The bores had linear long wave phase speeds
1040 approximately double that of the particle velocities within the bores. They exhibited
1041 typical characteristics of internal bores including a strong rotor at the leading edge
1042 and alternating upwards and downwards vertical velocities during the passage of the
1043 following internal waves of elevation. Their regular occurrence demonstrates the
1044 consistency of the lee wave generation and subsequent evolution into a propagating
1045 internal bore and suggests that the overall process may be implicated in the
1046 aggregation of apex predators, specifically the silvertip sharks observed there,
1047 around the seamount summit flanks where the lee waves are formed.

1048

1049 ***Acknowledgements***

1050 This work was supported by the Bertarelli Foundation and we thank them for their
1051 generous and sustained financial support in making the 2 cruises possible. Tom
1052 Letessier was the cruise leader for each cruise and we thank him for his organisation
1053 and support throughout both the planning and execution of each expedition. We
1054 further thank the crew of the BIOT Fisheries Patrol Vessel, Pacific Marlin, without
1055 whose assistance we would not have been able to execute such an ambitious
1056 observational programme. Our thanks particularly go to the captain, Neil Sandes,
1057 whose ship-driving skills were critical in mooring deployment and recovery, and chief
1058 engineer, Les Swart, whose knowledge and understanding ensured safe and
1059 effective deck operations throughout key deployments in the cruise. CCMP Version-

1060 2.0 vector wind analyses are produced by Remote Sensing Systems. Data are
1061 available at www.remss.com.

1062

1063

1064 **References**

1065

1066 Alexander, R. M., 2004: Hitching a lift hydrodynamically--in swimming, flying and
1067 cycling. *J. Biol.*, **3**, 7, doi:10.1186/jbiol5.

1068 Alford, M. H., J. M. Klymak, and G. S. Carter, 2014: Breaking internal lee waves at
1069 Kaena Ridge, Hawaii. *Geophys. Res. Lett.*, **41**, 906–912,
1070 doi:10.1002/2013GL059070.

1071 Barnett, A., G. Abrantes, K., J. Seymour, and R. Fitzpatrick, 2012: Residency and
1072 Spatial Use by Reef Sharks of an Isolated Seamount and Its Implications for
1073 Conservation. *PlosOne*, **7**, doi:10.1371/journal.pone.0036574.

1074 Boehlert, G. W., 1988: Current-topography interactions at mid-ocean seamounts and
1075 the impact on pelagic ecosystems. *GeoJournal*, **16**, 45–52,
1076 doi:10.1007/BF02626371.

1077 Buijsman, M. C. and Coauthors, 2014: Three-Dimensional Double-Ridge Internal
1078 Tide Resonance in Luzon Strait. *J. Phys. Oceanogr.*, **44**, 850–869,
1079 doi:10.1175/JPO-D-13-024.1.

1080 Cabeza, C. and Coauthors, 2009: Two-layer stratified flows over pronounced
1081 obstacles at low-to-intermediate Froude numbers. *Phys. Fluids*, **21**,
1082 doi:10.1063/1.31110108.

1083 carter, glenn, and michael gregg, 2002: intense, variable mixing near the head of
1084 monterey submarine canyon. *J. Phys. Oceanogr.*, **32**, 3145–3165.

1085 Chapman, D. C., and D. B. Haidvogel, 1992: Formation of Taylor caps over a tall
1086 isolated seamount in a stratified ocean. *Geophys. Astrophys. Fluid Dyn.*, **64**, 31–
1087 65, doi:10.1080/03091929208228084.

1088 Currie, J. C., M. Lengaigne, J. Vialard, D. M. Kaplan, O. Aumont, S. W. a Naqvi, and
1089 O. Maury, 2013: Indian ocean dipole and El Niño/Southern Oscillation impacts
1090 on regional chlorophyll anomalies in the Indian Ocean. *Biogeosciences*, **10**,
1091 6677–6698, doi:10.5194/bg-10-6677-2013.

1092 Embling, C. B., J. Sharples, E. Armstrong, M. R. Palmer, and B. E. Scott, 2013: Fish
1093 behaviour in response to tidal variability and internal waves over a shelf sea
1094 bank. *Prog. Oceanogr.*, **117**, 106–117, doi:10.1016/j.pocean.2013.06.013.

1095 Eriksen, C. C., 1998: Internal wave reflection and mixing at Fieberling Guyot. *J.*
1096 *Geophys. Res.*, **103**, 2977–2994, doi:10.1029/97JC03205.

1097 Genin, A., 2004: Bio-physical coupling in the formation of zooplankton and fish
1098 aggregations over abrupt topographies. *J. Mar. Syst.*, **50**, 3–20,
1099 doi:10.1016/j.jmarsys.2003.10.008.

1100 Genin, A., and G. W. Boehlert, 1985: Dynamics of temperature and chlorophyll
1101 structures above a seamount: An oceanic experiment. *J. Mar. Res.*, **43**, 907–
1102 924, doi:10.1357/002224085788453868.

1103 van Haren, H., and L. Gostiaux, 2010: A deep-ocean Kelvin-Helmholtz billow train.
1104 *Geophys. Res. Lett.*, **37**, 1–5, doi:10.1029/2009GL041890.

1105 Van Haren, H., 2005: Internal waves near the buoyancy frequency in a narrow wave-
1106 guide. *J. Sea Res.*, **53**, 121–129, doi:10.1016/j.seares.2004.06.001.

- 1107 Van Haren, H., U. Hanz, H. de Stigter, F. Mienis, and G. Duineveld, 2017: Internal
 1108 wave turbulence at a biologically rich Mid-Atlantic seamount. *PLoS One*, **12**, 1–
 1109 16, doi:10.1371/journal.pone.0189720.
- 1110 Haury, L., C. Fey, C. Newland, and A. Genin, 2000: Zooplankton distribution around
 1111 four eastern North Pacific seamounts. *Prog. Oceanogr.*, **45**, 69–105,
 1112 doi:10.1016/S0079-6611(99)00051-8.
- 1113 Hearn, A., J. Ketchum, A. P. Klimley, E. Espinoza, and C. Peñaherrera, 2010:
 1114 Hotspots within hotspots? Hammerhead shark movements around Wolf Island,
 1115 Galapagos Marine Reserve. *Mar. Biol.*, **157**, 1899–1915, doi:10.1007/s00227-
 1116 010-1460-2.
- 1117 Henyey, F. S., and A. Hoering, 1997: Energetics of borelike internal waves. *J.*
 1118 *Geophys. Res.*, **102**, 3323–3330.
- 1119 Hermes, J. C., and C. J. C. Reason, 2008: Annual cycle of the South Indian Ocean
 1120 (Seychelles-Chagos) thermocline ridge in a regional ocean model. *J. Geophys.*
 1121 *Res. Ocean.*, **113**, 1–10, doi:10.1029/2007JC004363.
- 1122 Hosegood, P., and H. van Haren, 2004: Near-bed solibores over the continental
 1123 slope in the Faeroe-Shetland Channel. *Deep Sea Res. Part II Top. Stud.*
 1124 *Oceanogr.*, **51**, 2943–2971, doi:10.1016/j.dsr2.2004.09.016.
- 1125 Hosegood, P., and H. van Haren, 2006: Sub-inertial modulation of semi-diurnal
 1126 currents over the continental slope in the Faeroe-Shetland Channel. *Deep Sea*
 1127 *Res. Part I Oceanogr. Res. Pap.*, **53**, 627–655, doi:10.1016/j.dsr.2005.12.016.
- 1128 Johnston, T. M. S., and M. A. Merrifield, 2003: Internal tide scattering at seamounts,
 1129 ridges, and islands. *J. Geophys. Res.*, **108**, 3180, doi:10.1029/2002JC001528.
- 1130 Jones, A. R., P. Hosegood, R. B. Wynn, M. N. De Boer, S. Butler-cowdry, and C. B.
 1131 Embling, 2014: Fine-scale hydrodynamics influence the spatio-temporal
 1132 distribution of harbour porpoises at a coastal hotspot. *Prog. Oceanogr.*,
 1133 doi:10.1016/j.pocean.2014.08.002.
- 1134 Klimley, A. P., and D. R. Nelson, 1984: Diel movement patterns of the scalloped
 1135 hammerhead shark (*Sphyrna lewini*) in relation to El Bajo Espiritu Santo: a
 1136 refuging central-position social system. *Behav. Ecol. Sociobiol.*, **15**, 45–54,
 1137 doi:10.1007/BF00310214.
- 1138 Klymak, J. M., S. M. Legg, and R. Pinkel, 2010a: High-mode stationary waves in
 1139 stratified flow over large obstacles. *J. Fluid Mech.*, **644**, 321–336,
 1140 doi:10.1017/S0022112009992503.
- 1141 Klymak, J. M., S. Legg, and R. Pinkel, 2010b: A Simple Parameterization of
 1142 Turbulent Tidal Mixing near Supercritical Topography. *J. Phys. Oceanogr.*, **40**,
 1143 2059–2074, doi:10.1175/2010JPO4396.1.
- 1144 LeBlond, P. H., and L. A. Mysak, 1978: *Wave in the Ocean*. Elsevier Scientific
 1145 Publishing Company, 602 pp.
- 1146 Legg, S., and K. M. H. Huijts, 2006: Preliminary simulations of internal waves and
 1147 mixing generated by finite amplitude tidal flow over isolated topography. *Deep.*
 1148 *Res. Part II Top. Stud. Oceanogr.*, **53**, 140–156, doi:10.1016/j.dsr2.2005.09.014.
- 1149 Legg, S., and J. Klymak, 2008: Internal Hydraulic Jumps and Overturning Generated
 1150 by Tidal Flow over a Tall Steep Ridge. *J. Phys. Oceanogr.*, **38**, 1949–1964,
 1151 doi:10.1175/2008JPO3777.1.
- 1152 Letessier, T. B., M. J. Cox, J. J. Meeuwig, P. H. Boersch-Supan, and A. S. Brierley,
 1153 2016: Enhanced pelagic biomass around coral atolls. *Mar. Ecol. Prog. Ser.*, **546**,
 1154 271–276, doi:10.3354/meps11675.
- 1155 Liao, J. C., 2007: A review of fish swimming mechanics and behaviour in altered
 1156 flows. *Philos. Trans. R. Soc. B Biol. Sci.*, **362**, 1973–1993,

1157 doi:10.1098/rstb.2007.2082.

1158 Mayer, F. T., and O. B. Fringer, 2017: An unambiguous definition of the Froude
1159 number for lee waves in the deep ocean. *J. Fluid Mech.*, **831**, 1–9,
1160 doi:10.1017/jfm.2017.701.

1161 Morato, T., S. D. Hoyle, V. Allain, and S. J. Nicol, 2010: Seamounts are hotspots of
1162 pelagic biodiversity in the open ocean. *Proc. Natl. Acad. Sci.*, **107**, 9707–9711,
1163 doi:10.1073/pnas.0910290107.

1164 Morel, A., H. Claustre, and B. Gentili, 2010: The most oligotrophic subtropical zones
1165 of the global ocean: Similarities and differences in terms of chlorophyll and
1166 yellow substance. *Biogeosciences*, **7**, 3139–3151, doi:10.5194/bg-7-3139-2010.

1167 Olson, R. S., A. Hintze, F. C. Dyer, D. B. Knoester, and C. Adami, 2012: Predator
1168 confusion is sufficient to evolve swarming behavior. doi:10.1098/rsif.2013.0305.

1169 Palmer, M. R., M. E. Inall, and J. Sharples, 2013: The physical oceanography of
1170 Jones Bank: A mixing hotspot in the Celtic Sea. *Prog. Oceanogr.*, **117**, 9–24,
1171 doi:10.1016/j.pocean.2013.06.009.

1172 Pawlowicz, R., B. Beardsley, and S. Lentz, 2002: Classical tidal harmonic analysis
1173 including error estimates in MATLAB using T_TIDE. *Comput. Geosci.*, **28**, 929–
1174 937, doi:10.1016/S0098-3004(02)00013-4.

1175 Pinkel, R., M. Buijsman, and J. Klymak, 2012: Breaking Topographic Lee Waves in a
1176 Tidal Channel in Luzon Strait. *Oceanography*, **25**, 160–165,
1177 doi:10.5670/oceanog.2012.51.

1178 Pollard, R., and J. Read, 2017: Circulation, stratification and seamounts in the
1179 Southwest Indian Ocean. *Deep. Res. Part II Top. Stud. Oceanogr.*, **136**, 36–43,
1180 doi:10.1016/j.dsr2.2015.02.018.

1181 Praveen Kumar, B., J. Vialard, M. Lengaigne, V. S. N. Murty, G. R. Foltz, M. J.
1182 McPhaden, S. Pous, and C. de Boyer Montégut, 2014: Processes of interannual
1183 mixed layer temperature variability in the thermocline ridge of the Indian Ocean.
1184 *Clim. Dyn.*, 1–21, doi:10.1007/s00382-014-2059-y.

1185 Sharples, J., J. R. Ellis, G. Nolan, and B. E. Scott, 2013: Fishing and the
1186 oceanography of a stratified shelf sea. *Prog. Oceanogr.*, **117**, 130–139,
1187 doi:10.1016/j.pocean.2013.06.014.

1188 Sheppard, C. R. C. and Coauthors, 2012: Reefs and islands of the Chagos
1189 Archipelago, Indian Ocean: Why it is the world's largest no-take marine
1190 protected area. *Aquat. Conserv. Mar. Freshw. Ecosyst.*, **22**, 232–261,
1191 doi:10.1002/aqc.1248.

1192 da Silva, J. C. B., M. C. Buijsman, and J. M. Magalhaes, 2015: Internal waves on the
1193 upstream side of a large sill of the Mascarene Ridge: a comprehensive view of
1194 their generation mechanisms and evolution. *Deep Sea Res. Part I Oceanogr.*
1195 *Res. Pap.*, **99**, 87–104, doi:10.1016/j.dsr.2015.01.002.

1196 Stashchuk, N., M. Inall, and V. Vlasenko, 2007: Analysis of Supercritical Stratified
1197 Tidal Flow in a Scottish Fjord. *J. Phys. Oceanogr.*, **37**, 1793–1810,
1198 doi:10.1175/JPO3087.1.

1199 Stevens, C., M. Consalvey, J. Devine, and M. Clark, 2014: Mixing and transport near
1200 the shallow-crested Rumble III seamount and the implications for plankton
1201 distribution. *New Zeal. J. Mar. Freshw. Res.*, **48**, 194–215,
1202 doi:10.1080/00288330.2013.872154.

1203 Thiebault, A., M. Semeria, C. Lett, and Y. Tremblay, 2016: How to capture fish in a
1204 school? Effect of successive predator attacks on seabird feeding success. *J.*
1205 *Anim. Ecol.*, **85**, 157–167, doi:10.1111/1365-2656.12455.

1206 Thompson, R. O. R. Y., and T. J. Golding, 1981: Tidally induced “upwelling” by the

1207 Great Barrier Reef. *J. Geophys. Res.*, **86**, 6517, doi:10.1029/JC086iC07p06517.
1208 Thorpe, S. A., 1977: Turbulence and Mixing in a Scottish Loch. *Philos. Trans. R.*
1209 *Soc. London*, **286A**, 125–181.
1210 Tickler, D. M., T. B. Letessier, H. J. Koldewey, and J. J. Meeuwig, 2017: Correction:
1211 Drivers of abundance and spatial distribution of reef-associated sharks in an
1212 isolated atoll reef system (PLoS ONE (2017) 12:5 (e0177374) DOI:
1213 10.1371/journal.pone.0177374). *PLoS One*, **12**, 1–18,
1214 doi:10.1371/journal.pone.0186560.
1215 Turnewitsch, R., M. Dumont, K. Kiriakoulakis, S. Legg, C. Mohn, F. Peine, and G.
1216 Wolff, 2016: Tidal influence on particulate organic carbon export fluxes around a
1217 tall seamount. *Prog. Oceanogr.*, **149**, 189–213,
1218 doi:10.1016/j.pocean.2016.10.009.
1219 Vialard, J., G. R. Foltz, M. J. McPhaden, J. P. Duvel, and C. de Boyer Montégut,
1220 2008: Strong Indian Ocean sea surface temperature signals associated with the
1221 Madden-Julian Oscillation in late 2007 and early 2008. *Geophys. Res. Lett.*, **35**,
1222 1–5, doi:10.1029/2008GL035238.
1223 Webber, B. G. M., A. J. Matthews, K. J. Heywood, J. Kaiser, and S. Schmidtke,
1224 2014: Seaglider observations of equatorial Indian Ocean Rossby waves
1225 associated with the Madden-Julian Oscillation. *J. Geophys. Res. Ocean.*, **119**,
1226 3714–3731, doi:10.1002/2013JC009657. Received.
1227 White, M., and C. Mohn, 2004: Seamounts: a review of physical processes and their
1228 influence on the seamount ecosystem. *Oasis Rep. Contract*,.
1229 Wunsch, C., and R. Ferrari, 2004: Vertical Mixing, Energy, and the General
1230 Circulation of the Oceans. *Annu. Rev. Fluid Mech.*, **36**, 281–314,
1231 doi:10.1146/annurev.fluid.36.050802.122121.
1232